Revista Mexicana de Astronomía y Astrofísica, 61, 98-119, (2025)
 https://doi.org/10.22201/ia.01851101p.2025.61.02.09

Physical Properties of H II Regions at Sub-kpc Scales Using Integral Field Spectroscopy on IC 342

J. K. Barrera-Ballesteros[1], S. F. Sánchez[2], K. Kreckel[3], A. Lugo-Aranda[1], H. Ibarra-Medel[1], L. Carigi[1], N. Drory[4], D. Bizyaev[5,6], J. E. Méndez Delgado[3] and Guillermo Blanc[7,8]

[1]*Universidad Nacional Autónoma de México, Instituto de Astronomía, AP 70-264, CDMX 04510, México.*
[2]*Universidad Nacional Autónoma de México, Instituto de Astronomía, AP 70-264, CDMX 04510, México.*
[3]*Astronomisches Rechen-Institut, Zentrum für Astronomie der Universität Heidelberg, Mönchhofstraße 12-14, 69120 Heidelberg, Germany.*
[4]*University of Texas at Austin, McDonald Observatory, 1 University Station, Austin, TX 78712, USA.*
[5]*Apache Point Observatory and New Mexico State University, P.O. Box 59, Sunspot, NM 88349-0059, USA.*
[6]*Sternberg Astronomical Institute, Moscow State University, Moscow, Russia.*
[7]*The Observatories of the Carnegie Institution for Science, 813 Santa Barbara St., Pasadena 91101, CA, USA.*
[8]*Departamento de Astronomía, Universidad de Chile, Camino del Observatorio 1515, Las Condes, Santiago, Chile.*

Keywords: *TBD*

Abstract

In this study, we use Integral Field Spectroscopic (IFS) observations for one of the closest galaxies to us, the grand design spiral IC 342, to derive the physical properties of H II regions at sub-kpc scales. To our knowledge, the IFS data represent the most comprehensive observational effort in the optical range for this galaxy. The final IFS datacube consists of 349 individual pointings using IFS instrumentation from the SDSS-IV MaNGA survey. Using a prototype of the data analysis pipeline that will be devoted to the SDSS-V Local Volume Mapper (LVM) survey, we measured different observables from the optical emission line. In particular, using the flux map of the Hα emission line, we derived the location and size of H II region candidates for IC 342. Using the integrated flux for different emission lines within each region, we derived the radial distribution of different physical properties from the ionized gas (e.g., optical extinction, Hα luminosity, oxygen abundance, etc.). Compared with larger samples of galaxies with IFS data, our results suggest that the physical properties of the ionized gas of IC 342 are similar to those of galaxies with similar stellar masses in the nearby universe.

Resumen

En este trabajo presentamos el análisis de las propiedades físicas de regiones H II a escalas de sub-kpc en una de las galaxias más cercanas a nosotros, IC 342, usando datos de espectroscopía de campo integral (IFS por sus siglas en inglés). Estos datos representan las observaciones más completas en el óptico de esta galaxia. El cubo de datos está compuesto por 349 observaciones individuales del cartografiado SDSS-IV MaNGA. Para el análisis de este cubo de datos usamos un prototipo del dataducto de análisis del cartografiado SDSS-V LVM, con el cual estimamos las propiedades de las líneas de emisión. En particular, usando el mapa de la línea de emisión de Hα determinamos la ubicación y el tamaño de candidatos a regiones H II. Usando las propiedades integradas para cada candidato estimamos la distribución radial para un gran número de propiedades físicas (e.g., extinción, luminosidad de Hα, abundancia de oxígeno, etc.). Comparando con galaxias de masa estelar similar y observadas con IFS, nuestros resultados muestran que las propiedades del gas ionizado para IC 342 son semejantes con dichas galaxias.

Corresponding author: J. K. Barrera-Ballesteros *E-mail address:* jkbarrerab@astro.unam.mx
Received: November 1, 2023 **Accepted:** Jul 4, 2025

1. Introduction

A theoretical H II region is a sphere of gas that surrounds young massive stars (mostly O and B type). The UV emission from these stars ionizes this gas, which cools down through emission lines, some of the brightest in the optical. Since OB stars are short-lived (< 15 Myr), the observed emission from these regions has often been used to trace recent star formation. Furthermore, thanks to the emission by the ionized gas contained in these regions, we are able to gain deep knowledge of, for instance, the luminosity function of the Hα emission line (which in turn traces the massive end of the initial mass function), the chemical content of the interstellar medium (ISM), or their dynamical stage. The size of an H II region is variable, from a few to hundreds of parsecs (e.g., the Orion Nebula and NGC 5471, from ∼8 pc to ∼1 kpc, respectively, Anderson, 2014; García-Benito et al., 2011). Aggregations of these large H II regions are considered giant H II regions, usually

observed in star-forming spirals (e.g., Hodge & Kennicutt, 1983; Dottori & Copetti, 1989; Knapen, 1998).

Observationally, these giant H II regions are usually traced as clumpy Hα emission across the optical extension of late-type galaxies (e.g., Kennicutt & Evans, 2012, and references therein). The galactocentric distribution of these regions is usually quantified by a radial gradient, suggesting that in most spirals, at their center the Hα flux of these regions is larger than that of regions located at the outskirts (e.g., Knapen et al., 2004; Bigiel et al., 2008). Using Hα narrow-band imaging it is possible to characterize the distribution of H II regions in a galaxy via the Hα luminosity function (e.g., González Delgado & Pérez, 1997; Bradley et al., 2006). Using long-slit spectroscopy, it has been possible to trace other physical properties of these regions in reduced samples of spiral galaxies, such as chemical abundances, electronic density, and the ionization parameter (e.g., Pilyugin & Grebel, 2016).

In recent years, extragalactic astronomy has witnessed a revolution in optical observations, thanks to the Integral Field Spectroscopic (IFS) technique applied to thousands of galaxies in the nearby Universe. Large IFS surveys such as CALIFA (Sánchez et al., 2012), MaNGA (Bundy et al., 2015), SAMI (Croom et al., 2012), and AMUSING++ (López-Cobá et al., 2017) have shown the spatially resolved properties of the demographics of galaxies in Of particular interest is the radial distribution of physical properties of the ionized gas derived from the emission line parameters in the optical (e.g., Sánchez-Menguiano et al., 2018; López-Cobá et al., 2017; Espinosa-Ponce et al., 2022; Barrera-Ballesteros et al., 2023). Given the success of these large IFS surveys, different research groups have employed different IFS techniques to map the properties of the ionized gas in nearby galaxies, reaching superb spatial resolutions (on the order of tens of pc). Among these different IFS surveys, the TYPHOON, SIGNALS, and PHANGS surveys are noteworthy (D'Agostino et al., 2018; Rousseau-Nepton et al., 2019; Emsellem et al., 2022).

Although there are dedicated IFS studies to explore the properties of H II regions in galaxies in the local universe ($D < 5$ Mpc), these are rather scarce. Using the MUSE instrument, it has been possible to explore the physical properties of H II regions at sub kpc scales in the LMC (McLeod et al., 2019), NGC 300 (McLeod et al., 2020, 2021), NGC 7793 (Della Bruna et al., 2020, 2021), and M83 (Della Bruna et al., 2022). These studies mainly focused on exploring how stellar feedback from recent star formation in H II regions affects the kinematics of the interstellar medium. Such studies are of great importance to bridge the gap between the observations at sub-kpc scales and those scaling relations between the star formation and the dynamical pressure at kpc scales for hundreds of galaxies (Barrera-Ballesteros et al., 2023). However, they lack a deep exploration of the physical properties of the ISM for H II regions at sub-kpc scales. With this work, we aim to shed some light on the radial distribution of the physical parameters at these physical scales derived from the emission lines in the optical.

In this study, we focused on IC 342. This galaxy is the closest grand-design spiral to the Milky Way (~3.3 Mpc Saha et al., 2002). Therefore, it was mapped at different wavelengths. From *WISE* data Jarrett et al. (2013) derived its total stellar mass ($\log(M_\star/M_\odot) \sim 10.8$, but see Zibetti et al., 2009; Zhu et al., 2010, for other estimations), and total star formation rate ($\sim 2.4 M_\odot$ yr^{-1}, see also Kennicutt et al., 2011). Its molecular and neutral gas content has also been extensively mapped either in its nucleus and arms (e.g., Rickard & Palmer, 1981; Ishizuki et al., 1990; Crosthwaite et al., 2000; Kuno et al., 2007). However, despite these studies, there have been few studies on the properties of ionized gas in IC 342. The only reported measurements of the emission line fluxes in four H II regions at different radii of this galaxy come from long-slit spectroscopy (McCall et al., 1985). Using these observations, Pilyugin et al. (2004) derived the oxygen abundance gradient for this galaxy. In this work, we present the largest integral field spectroscopic study of IC 342 in the optical. We took advantage of ancillary observations from the MaNGA survey (Bundy et al., 2015) devoted to mosaicing this galaxy. In particular, we focus on the radial distribution of the physical parameters that could be derived from the observed properties of the different emission lines in the optical within a given H II region. Owing to its high angular resolution, the current dataset also provides us with a unique opportunity to test the data-analysis pipeline that is being used to determine the physical properties in the Local Volume Mapper (Drory et al., 2024), an ongoing SDSS-V survey (Kollmeier et al., 2017) aimed at mapping the physical properties of the ionized gas within the Milky Way and galaxies included in the Local Volume (Konidaris et al., 2020).

The remainder of this paper is organized as follows: In § 2 we present the IFS observations of IC 342 as well as the data analysis pipeline used to derive the maps of the quantities from the observations. In § 3 we describe the method used to estimate the position and size of the H II regions, the derived physical quantities for each region, and their classification in an emission-line diagnostic diagram. In § 4 we present the galactocentric distribution of the physical properties derived from the H II regions. In § 5 we present the Hα luminosity function for IC 342 derived from the H II regions. In § 6 we explore the correlations between the radial residuals of the derived physical properties. In § 7 we summarize and discuss our results in the framework of recent IFS surveys.

2. Data

2.1. IFS observations as MaNGA ancillary program

The observations to map the disk of IC 342 were part of an ancillary program included in the MaNGA survey (PI. K. Kreckel). The MaNGA (Mapping Nearby Galaxies at Apache Point Observatory; Bundy et al., 2015) survey

was part of the fourth generation of surveys included in the Sloan Digital Sky Survey (SDSS-IV; Blanton et al., 2017). This survey observed more than 10000 galaxies in the nearby universe using the IFS technique. Here, we briefly review the main features of this survey. Observations were conducted at the Apache Point Observatory using a 2.5-m telescope (Gunn et al., 2006). It used two spectrographs from the BOSS survey (Baryon Oscillation Spectroscopic Survey Smee et al., 2013). BOSS spectrographs achieve a nominal spectral resolution of $R \equiv \lambda/\Delta\lambda \sim 1900$ covering a large portion of the optical spectra (from 3000 to 10000 Å). These spectrographs were fed by joined fibers in bundles distributed in a hexagon-like array (also known as integral field units, IFUs). The number of fibers in a given bundle, or IFU, varied from 19 to 127. Because the diameter of each fiber is $\sim 2''$, the field of view (FoV) for each IFU varies between $12''$and $32''$. Observations of MaNGA targets were performed using a plugplate system, where the locations for each IFU (and corresponding sky fibers), 12 spectrophotometric standard stars, and 16 guide stars were pre-drilled. This provides the necessary observations for the acquisition, guiding, and dithering of targets, along with all the calibration data needed in the data reduction pipeline. A detailed description of the instrumentation used in the survey can be found in Drory et al. (2015). The reader is referred to Law et al. (2016) for a detailed explanation of the data strategy (acquisition, reduction, etc.). The MaNGA reduction pipeline includes wavelength calibration, corrections from fiber-to-fiber transmission, subtraction of the sky spectrum, and flux calibration (Yan et al., 2016). The final product is a datacube with x and y coordinates corresponding to the sky coordinates and the z-axis corresponding to the wavelength.

The IC 342 observations were taken as part of an ancillary program that was needed to provide additional MaNGA science targets when the Milky Way was above. IC 342 has been neglected in optical studies as it suffers from high foreground Milky Way extinction ($A_V = 1.530$; Schlafly & Finkbeiner 2011), but at a galactic latitude of ∼10 deg it was well situated for this ancillary program.

The goal was to produce a uniform, contiguous mosaic covering the central $11' \times 11'$ (10 kpc × 10 kpc) region. This reaches 0.25 $R_{25} \approx 1.25$ R_e ($R_{25} = 22'$), which is well matched to the primary MaNGA sample. Each of these pointings results in a datacube with a spaxel size of $0.5''$(the spatial resolution is given by the average size of the PSF per fiber, which is typically $2.54''$, Law et al., 2016). Given the distance of IC 342 this corresponds to a spatial resolution of ∼ 32 pc. Thus, these IFS data represent observations with significantly higher physical resolution than typical MaNGA targets (∼3 kpc), surpassing even what is achieved with other nearby galaxy surveys, such as PHANGS-MUSE (∼70 pc; Emsellem et al. 2022).

The final mosaic of IC 342 uses 49 plates and was observed between early 2017 and late 2021. Three pilot plates (plate numbers: 9673-9675) were initially observed to test the feasibility of this survey, with IFUs placed on HII regions that provided good radial and azimuthal coverage. A total of 46 plates (with plate numbers: 10141-10150, 10480-10491, 12027-12050) were used to uniformly mosaic the central 10 arcmin diameter disk of IC 342. In some cases, these overlapped with the positions of the IFUs in the pilot plates. Plate 10490 had one dropped IFU bundle, leading to a gap in coverage. An additional 15 plates were planned but not completed before the end of the MaNGA survey operations. Each plate was observed at three dither positions, following the standard MaNGA procedure to fill the interstitial regions(Law et al., 2016), and only the two largest IFUs were used (i.e., the bundles with 127 and 91 fibers). Individual IFU positions are tiled such that no gaps exist when all IFU fibers are combined into a single data cube. As a result, seven large contiguous regions were observed (Figure 1) with a total of over 10^5 spectra (including the dither positions).

Each of these plates was observed using the same strategy as a standard MaNGA plate; thus, it was possible to use the same data reduction pipeline as that used for the rest of the survey. The diameter of the IC 342 is sufficiently small that sky fibers can be placed successfully for each IFU within the $14'$patrol field. Exposure times in the pilot observations were limited to a total of 1 h (two visits of 30 min, with 10 min per dither), but in the full survey, the total integration time was 1.5 h (two visits of 45 min, with 15 min per dither).

2.2. Deriving emission line properties using the LVM-DAP

As mentioned in the previous section, given the close distance of IC 342, the IFS dataset provided by the MaNGA observations has a superb angular resolution, making it very suitable for using an analysis pipeline dedicated to IFS datasets from Local Volume galaxies. Therefore, we used the IFS dataset from IC 342 as a test-bed for the data analysis pipeline (DAP). The DAP is used to analyze the data observed by the Local Volume Mapper (LVM) survey, which is part of the fifth generation of the SDSS collaboration. The details of the LVM-DAP are described in (Sánchez et al., 2025), and its preliminary results are presented in (Drory et al., 2024). Here, we provide a brief description of the main features of this DAP, focusing on the extraction of physical properties from ionized gas. Although with significant variations, the LVM-DAP follows a methodology similar to that of the `pyPipe3D` pipeline (Lacerda et al., 2022). This DAP is an update of the pipeline `Pipe3D` (Sánchez et al., 2015a, 2016), which has been widely used to extract two-dimensional distributions of physical properties from both the stellar and ionized gas components for heterogeneous datasets (e.g., CALIFA, MaNGA, AMUSING++).

In contrast to nearby galaxies, for those galaxies included in the Local Volume (including the Milky Way), it is no longer valid to assume that the stellar continuum of a portion of a galaxy is composed of the linear combination

of single stellar population spectra (SSPs). Thus, the LVM-DAP derives the stellar population using a technique called resolved stellar population (RSP) to estimate the best stellar continuum of the data observed at the LVM. A detailed description of this extraction and the physical properties derived for the stellar component of the spectra will be described elsewhere (Mejia et al., in prep.) In this case, the estimation of the best stellar continuum is no longer based on a linear combination of different SSPs but on a library of individual stellar spectra covering a wide range of stellar properties (e.g., effective temperature, gravity, and chemical abundances). For each spectrum in each reduced datacube. The DAP starts by deriving the systemic velocity, velocity dispersion, and optical extinction from the stellar continuum by fitting only four stellar spectra. Once the best estimations for these parameters were derived, a stellar model was derived and subtracted from the observed spectra, and a set of Gaussian profiles was fitted to a pre-defined set of emission lines. These Gaussian profiles are then subtracted from the observed spectra, and a new fit of the stellar component is performed using a large set of stellar spectra, yielding the final continuum model. The remaining "gas-only" spectrum was then analyzed using a weighted-moment non-parametric procedure to estimate the integrated flux, velocity, velocity dispersion, and EW of a pre-defined set of 192 emission lines. Contrary to DAP, where the data are stored in the form of RSS tables, the data for IC 342 are stored in the usual format of the MaNGA survey for each pointing, as maps for each of the properties for each of the analyzed emission lines. Furthermore, for each property derived by the DAP in IC 342 we perform a mosaic using the maps from individual pointings. These maps have a scale of 1 arcsec per pixel. For the details of the algorithms and their implementation we refer the reader to Sanchez (in prep) and Lacerda et al. (2022) [1]. In Figure 1 we show the map of the Hα line, whereas in Appendix A we present the maps of other strong emission lines. The maps of the physical properties from all the pointings can be found in https://ifs.astroscu.unam.mx/MaNGA/IC342/output_dap/.

2.3. The AMUSING++ sample

To compare the trends derived for the H II regions within IC 342 with respect to the sample of H II regions located in a larger sample of galaxies, we used the AMUSING++ sample (López-Cobá et al., 2020). This sample is an extension of the All-Weather MUse Supernova Integral Field Nearby Galaxies survey (AMUSING Galbany et al., 2016, 2020). This compilation of galaxies observed with the MUSE instrument includes observations from a wide variety of scientific goals (see details in López-Cobá et al., 2020). Although the initial compilation included 635 galaxies (López-Cobá et al., 2020), an updated sample comprised 678 galaxies (Lugo-Aranda et al., 2024). The galaxies in the AMUSING++ sample were selected so that the MUSE field of view had a good spatial coverage ($\sim$ 2 effective radius), and that they are nearby galaxies ($0.004 < z < 0.06$). This sample has significant coverage in both stellar masses and morphology (see details in Lugo-Aranda et al., 2024). The inclusion of nearby galaxies in the sample ensures a good spatial resolution ($\sim$ 100 to 1000 pc). Using the latest compilation of the AMUSING++ sample, Lugo-Aranda et al. (2024) characterized the physical properties of more than 52 000 H II regions. We used the data for these H II regions to compare them with the trends observed in the H II regions located in IC 342 (see § 3.3).

3. Analysis

3.1. Detecting HII regions using PyHIIEXTRACTOR

With maps of the physical properties derived from the different emission lines, we used the Hα emission mosaic to determine the locations and sizes of the H II regions. To do this, we used the code PyHIIEXTRACTOR (Lugo-Aranda et al., 2022). This code detects and extracts the properties of clumpy regions considered as H II regions using an Hα emission-line image. If IFU data are available for that image, this code can also extract the physical properties within each of the detected H II regions (e.g., physical properties for each observed emission line and properties from the stellar continuum). Although PyHIIEXTRACTOR also models the Hα diffuse emission (also known as diffuse ionized gas, DIG), in this study, we focus only on the physical properties of the H II regions. In a future study, we will explore the properties of DIG for IC 342. To proceed with the estimation of the location and size of the H II regions, the code requires a set of initial values. We refer the reader to Lugo-Aranda et al. (2022) for a detailed description of those parameters; here, we describe the parameters we use to extract the physical information of the H II regions. For this study, we systematically varied (i) the Hα flux threshold above which the code detects clumpy regions and (ii) the maximum size of the detected H II regions. We also set the code to search for H II regions with 300 different sizes, varying from one spaxel to the maximum size. By visually inspecting the resulting sizes and locations of the H II regions derived by PyHIIEXTRACTOR, we find that appropriate initial values for the code are a value for (i) of $\sim 5 \times 10^{-18}$ erg s^{-1} Å^{-1} and for (ii) the spatial resolution of the observations (set by the size of the fiber, $\sim 2.5''$). Because the range of sizes of the H II begins with one spaxel (which does not have a physical meaning), we discard regions with one spaxel of radius. We explore a wide range of maximum sizes for our H II regions; however, we find that having larger maximum sizes yields spurious large H II regions. In total, we detected 4701 clumpy regions; however, as described below, to guarantee that we have reliable measurements of the physical properties of the H II regions, we apply further selection criteria. In Figure 1 we display the locations and sizes of the H II regions for IC 342

[1] http://ifs.astroscu.unam.mx/pyPipe3D/

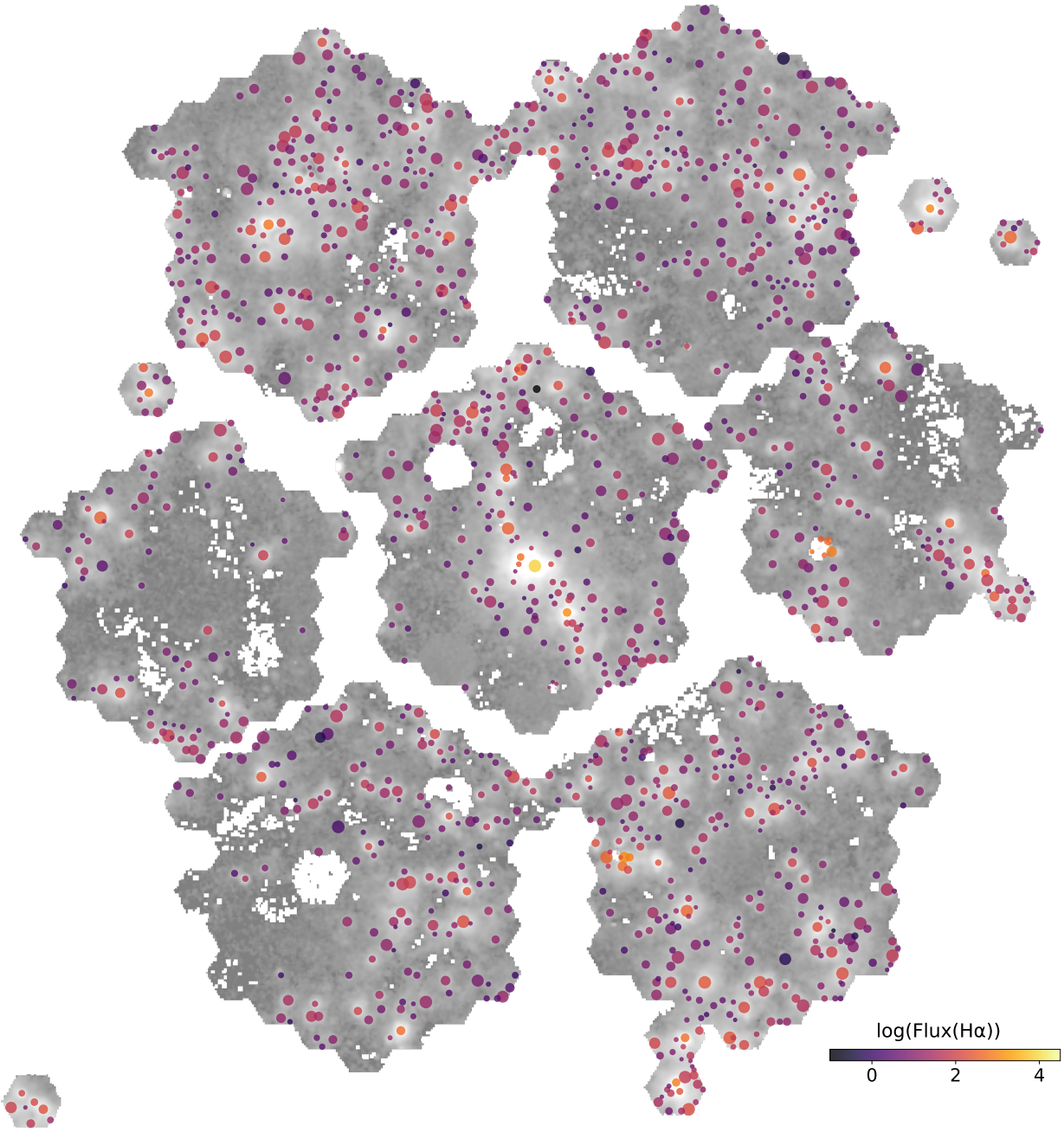

Figure 1. Flux of the Hα emission line from H II candidates detected by PYHIIEXTRACTOR overplotted over the Hα emission line map derived using the DRP-LVM.

as red circles. As expected, most of the H II regions are located within the arms of the galaxy.

To provide reliable estimations of the physical properties for each of the detected H II regions, we used the following criteria: each region should have (i) all the emission line fluxes with positive values, and (ii) the signal-to-noise ratio of the Hα emission line has to be larger than three. In the next section, we classify regions according to their location in their BPT diagram and their Hα equivalent width. From these criteria, we obtained a final sample of 1155 H II regions.

3.2. Derived Properties

For each of the selected H II regions, we used the integrated/averaged properties derived from the LVM-DAP within its radius. Thus, for each emission line, we spatially integrated the flux and averaged the other properties, such as the equivalent width and FWHM. Using this dataset, we derived the physical properties that we will cover in

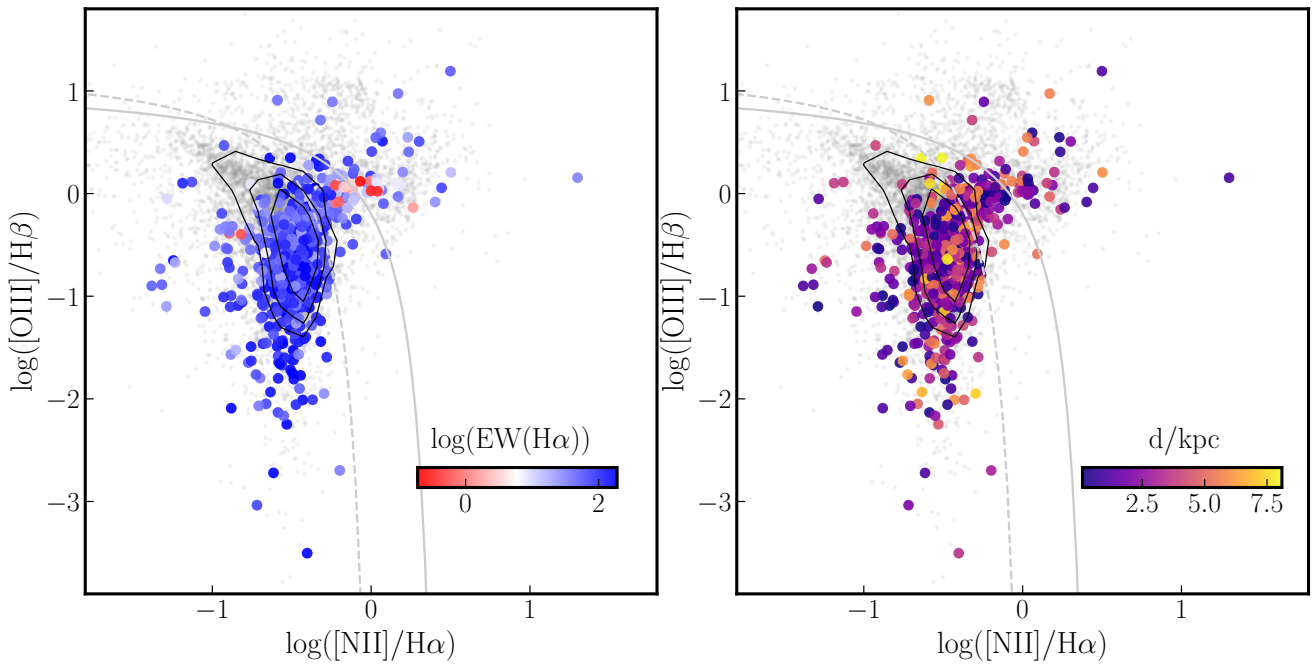

Figure 2. H II candidates in the BPT diagram. *Left:* Candidates color-coded by their Hα equivalent width. *Right:* Candidates color-coded by their galactocentric distance. The dots represent the properties of the AMUSING++ sample. In both panels, the solid and dashed lines represent the Kauffman and Kewley demarcation lines, respectively. We use this demarcations lines and the Hα equivalent width to select *bona fide* star-forming regions in IC 342.

this study. From the Hα/Hβ ratio, known as the Balmer decrement, we derived the optical extinction, A_V, following the prescription outlined by Catalán-Torrecilla et al. (2015). Using this estimation of A_V, we derived the dust-corrected Hα luminosity for each region. However, to derive other physical properties such as oxygen and nitrogen abundances, electronic density, and ionization parameter, we also use the integrated flux from other emission lines, including the optical range of the observations. We refer the reader to the study by Espinosa-Ponce et al. (2022) for a complete list of emission lines used in this study to derive the physical parameters mentioned above. We note that although there is a large list of oxygen abundance calibrators in this study, we use the one provided by Ho (2019). Finally, regarding the kinematic properties of each region, we averaged the systemic velocity and velocity dispersion.

3.3. The BPT diagnostic diagram and the classification of HII regions

Diagnostic diagrams have been widely used to classify galaxies and regions according to their ionizing sources. This is the case for the BPT diagram (Baldwin et al., 1981). In this section, we present the locations of the IC 342 candidates in the BPT diagram. Along with their EW(Hα), we used these line ratios to select the *bona fide* H II regions.

In Figure 2, we plot the H II candidates in the classical BPT diagram (i.e., [O III]/Hβ vs [N II]/Hα). For comparison, we also plotted the line ratios from the AMUSING++ sample. Although most of the regions from both samples are located in the so-called 'star-forming branch', we note that the AMUSING++ sample covers a wider dynamical range in the [N II]/Hα axis than the H II candidates from IC 342. This is related to the differences we find previously in the radial distribution of the O3N2 ratio in these two samples. Furthermore, there are also AMUSING++ candidates with larger values of the [O III]/Hβ ratio compared to those derived from the IC 342 sample. We suspect that this is due to regions with sources of ionization that are different from star formation. However, further exploration of the AMUSING++ sample of H II candidates is beyond the scope of this study and will be addressed elsewhere (Aranda-Lugo et al. in prep.)

A quantitative classification of the different ionization mechanisms is given by the demarcation lines proposed by Kauffmann et al. (2003); Kewley et al. (2001, see the dashed and solid lines in Figure 2, respectively). Galaxies/regions below these demarcation lines are usually classified as star-forming, while those above these demarcations could have different classifications (i.e., composite-like galaxy/regions if the line ratios are between these demarcations or AGN-like galaxy/region if the ratios are above the Kewley demarcation line). We find that the majority of regions lie below these demarcation lines in the BPT diagram (~80% and ~92% for the Kauffmann and Kewley demarcation lines, respectively).

The Hα equivalent width, along with the [N II]/Hα ratio, has also been used to characterize the ionization source of

galaxies/regions (e.g., Cid Fernandes et al., 2010; Lacerda et al., 2018). In the left panel of this figure, we color-code our candidates in the BPT diagram by their EW(Hα). We note that almost all the regions below these demarcation lines have large values of EW(Hα) with an average of ∼100 Å. Conversely, most of the regions with low EW(Hα) are above the demarcation line (∼40 Å). In comparison to the AMUSING++ sample, the IC candidates have large values of EW(Hα), both above and below the demarcation lines. The right panel of Figure 2, we color-code the candidates according to their galactocentric distance. We do not find a clear trend between the distance and location of the candidates in the BPT diagram. Regions above and below the demarcation line are distributed across the optical extension of the IC. Given that flux ratios above the Kewley demarcation line are typically associated with nuclear activity, this result suggests that a physical process other than nuclear activity could be responsible for the ionization in those regions.

Depending on the study, there are different thresholds for selecting star-forming galaxies/regions. Cid Fernandes et al. (2011) used as threshold EW(Hα) > 6 Å. In this study, we used a more conservative value to select star-forming regions (EW(Hα) > 14 Å Lacerda et al., 2020). Thus, to obtain *bona fide* H II regions from our sample of candidates, we selected those regions with flux ratios below the theoretical demarcation line proposed by Kewley et al. (2001), as well as regions with the aforementioned EW(Hα) values. Using these criteria from the sample of 1155 candidates in IC 342 we selected 960 star-forming regions. Although it is beyond the scope of this study, we note that for those nebulae that were selected as non-star-forming, a significant fraction are regions with low EW(Hα) below the Kewley demarcation line (121/195). This could indicate that the ionizing source is different from that expected from supernova remnants (e.g., Vicens-Mouret et al., 2023). Further studies are required to assess the true nature of the ionization of these sources.

4. Radial Distribution of Physical Parameters

4.1. Properties derived from Balmer lines

To obtain the Hα dust-corrected luminosity for our sample of H II regions, it is necessary to estimate the extinction using the Hα/Hβ ratio. In this section, we explore the radial distribution of extinction. We also explored the radial distribution of both the Hα line equivalent width and the Hα luminosity.

Optical Extinction, A_V: In Figure 3 we plot the radial distribution of A_V for the sample of H II candidates with a Hα/Hβ ratio larger than 2.86. First, we note that the average extinction derived from the Balmer decrement for these candidates is close to one, $A_V \sim 1.3$ mag, with a large scatter measured from the standard deviation, $A_V \sim 1.4$ mag. Although the distribution of extinctions presents a large scatter, once the extinctions are represented against the galactocentric distance of the regions, they

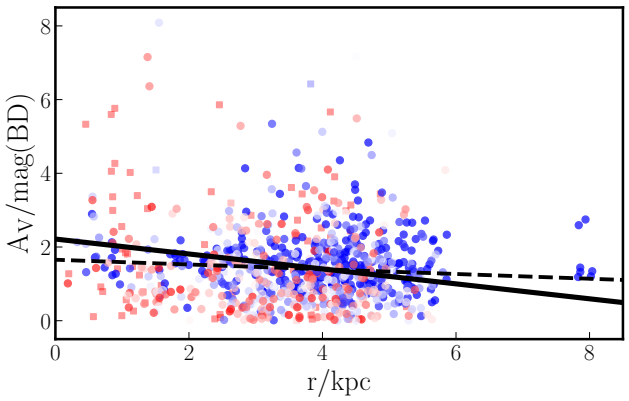

Figure 3. Radial distribution of the optical extinction, A_V, derived for the H II regions in IC 342. The symbols are color-coded according to their EW(Hα). The solid line represents the best-fit radial gradient for the data. In average, we do not find a significant variation of A_V for IC 342.

follow a decreasing trend. To further quantify this trend, we derived the radial gradient of the optical extinction by fitting a single-slope line to the dataset (black solid line in Figure 3). We found that the best slope and zero-point were -0.18 mag / kpc and 2.21 mag, respectively. We note that there are regions with an extinction significantly larger than the median value, or, in other words, significantly above the best-fit gradient. These high-extinction regions are across the extension of the galaxy, with no clustering at a specific galactocentric distance. We also note that these regions cover a wide range of values of EW(Hα), as seen by the color codes of the data points in Figure 3. In this figure, we also segregate the candidates according to the selection criteria described in § 3.3, that is, between star- and non-star-forming regions (circles and squares, respectively). We note that in the central region ($r < 2$ kpc), most of the regions with high extinction are non-star-forming candidates, whereas at larger radii, these regions are mostly star-forming. To further understand the origin of these regions with high extinction, we mapped the residuals of extinction with respect to its gradient, as shown in Figure 20. We note that some of these regions appear to be clustered towards the arms of IC 342 (e.g., the north-west at ∼ 4 kpc or the south-east at ∼ 8 kpc). In the following sections, we explore whether these atypical regions correlate with other properties of the regions.

EW(Hα): Contrary to the the optical extinction, we find that in general the radial distribution of the EW(Hα) from the H II candidates follows an increasing trend (see Figure 4). We plot this radial distribution, color-coded by the star formation status. We found that the star-forming regions followed a positive radial trend, in contrast to non-star-forming regions, which had a large scatter and no evident trend (green circles and pink squares, respectively). In contrast, when we derived the best single gradient for this radial distribution, we found that selecting only

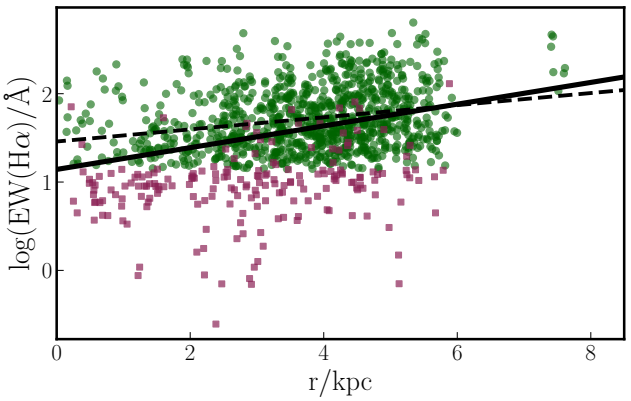

Figure 4. Radial distribution of the EW(Hα) for the H II candidates in IC 342. The green and pink symbols represent the star-forming and non-star-forming regions, respectively. The solid and dashed lines represent the best-fit radial gradient for the entire data and using only H II regions, respectively.

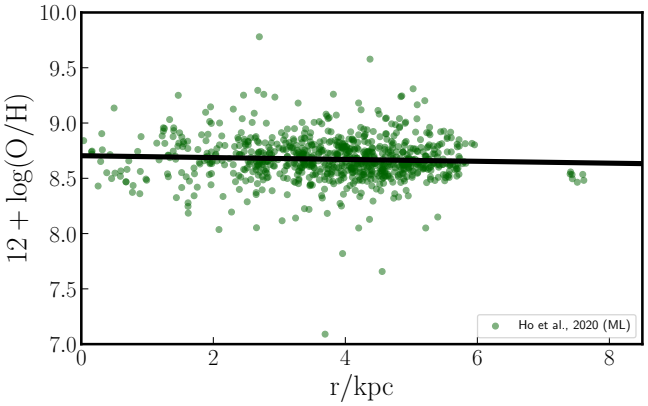

Figure 6. Radial distribution of the oxygen abundance using the calibrator from Ho (2019) for star-forming regions. The black solid line shows a best gradient fit representing the almost flat radial distribution of the oxygen abundance for the star-forming regions in IC 342.

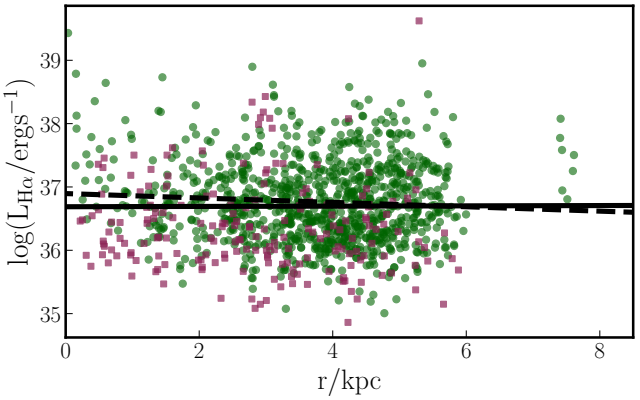

Figure 5. Radial distribution of the Hα luminosity. Colors of the symbols and lines are similar as those derived in Figure 4.

star-forming regions led to a shallower gradient than that derived using all H II candidates (dashed and solid lines, respectively). In Figure 21 we color-code the residual of the EW(Hα) with respect to the radial gradient derived above for each position and radius of the H II candidates. We find that the central star-forming regions are those with a larger enhancement of EW(Hα), whereas some of the external star-forming regions (e.g., at the outskirt north-west direction). On the other hand, we find that most non-star-forming regions have a deficit in their EW(Hα) in comparison to the derived gradient and are distributed in the central region of IC 342. In the next section, we explore how the residuals from this radial gradient correlate with other physical properties derived from the emission lines.

Hα luminosity: In Figure 5, we plot the radial distribution of these luminosities. They follow a rather flat distribution with respect to their galactocentric distances. When we segregated our sample into star- and non-star-forming regions, we did not find a significant difference between the radial distributions of their Hα luminosities. For a given galactocentric distance, both samples show a large scatter in their Hα luminosities. For the previous parameters, we derived the best radial gradient for these luminosities. We find a mild negative gradient, which becomes even flatter when we derive it using only star-forming regions (solid and dashed lines, respectively).

4.2. Oxygen Abundances

In Figure 6, we plot the radial distribution of oxygen abundance for the sample of star-forming regions in IC 342. As mentioned in § 3, from the large set of abundance calibrators, we use as a fiducial calibrator the one derived from Ho (2019). We note that the gradient provided by the best-fit is rather flat with a slightly negative slope. As with the other properties, we have mapped in Figure 22 shows the residuals of the oxygen abundance for each star-forming region, where it is possible to derive the oxygen abundance. We did not find a cluster or specific location of regions with an excess or deficit in their abundance. In § 6, we further explore how the radial residuals of different physical properties correlate with each other.

To quantify the impact of the abundance calibrators on the estimation of the best gradient, we used each of the calibrators presented in § 3 to derive the oxygen abundance gradient. In Figure 7 we plot the slope and zero-point from the best fit for the set of 23 calibrators. We note that, although there are significant variations in both parameters, the average value of the slope is consistent with a flat radial distribution of oxygen abundance. The central abundance given by the average zero-point is close to solar abundance. Finally, we note that the number of star-forming regions employed to estimate the best gradient varies depending on the calibrator. This difference in sampling is due to (i) the emission lines required to derive a specific calibrator and (ii) the dynamic range imposed for each of them.

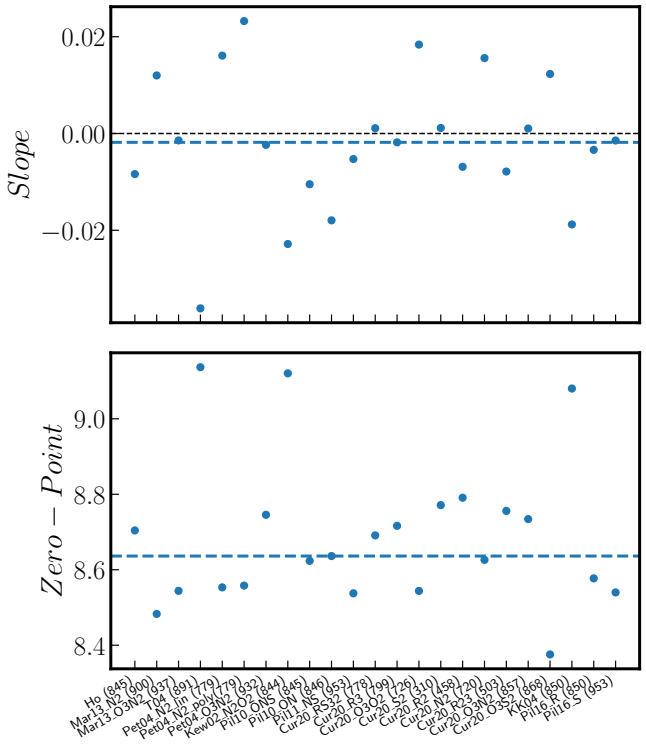

Figure 7. Best-fit parameters for the radial gradient of oxygen abundance using the set of calibrators described in § 3: slope and zero-point (top and bottom panels, respectively). In the top panel, the black dashed line represents a flat gradient, while the blue dashed line represents the average of the slopes from the different sets of calibrators. In the bottom panel, the blue dashed line represents the average of zero-points from the different calibrators. On average, the distribution of oxygen abundance in the star-forming galaxies of IC 342 is rather flat, with a central oxygen abundance close to solar. We describe the number of star-forming regions used for each calibrators in parenthesis.

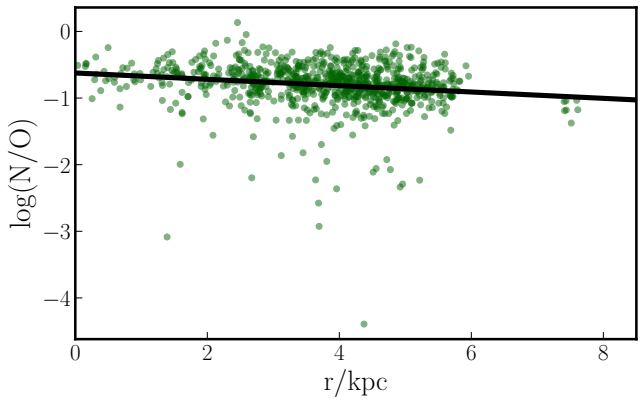

Figure 8. Radial distribution of the N/O ratio for star-forming regions.As for the oxygen abundance, the black line represent the best fit for this radial distribution.

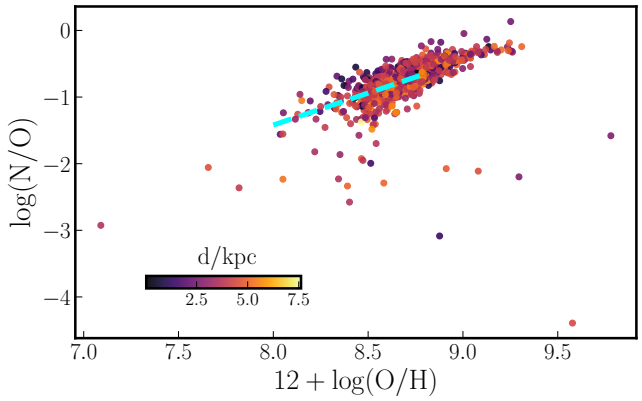

Figure 9. Nitrogen-to-oxygen ratio against the oxygen abundance ratio. The cyan-dashed line represents the best fit for these two parameters derived from H II regions observed in the CALIFA survey (Espinosa-Ponce et al., 2022). We note that in comparison to a large sample of regions, those from IC 342 have large N/O ratios.

4.3. N/O ratio

The measurement of chemical abundances from elements with different nucleosynthesis processes allows us to trace the scales of star formation in the evolution of IC 342. Short-lived massive stars are traced by oxygen abundance, whereas nitrogen abundance traces longer lifetimes and lower mass stars. As mentioned in § 3, the nitrogen abundance was measured using the calibrator presented in Pilyugin & Grebel (2016), whereas for the oxygen abundance, we used our fiducial calibrator (Ho, 2019).

In Figure 8, we plot the radial distribution of the N/O ratio for the sample of H II regions detected in IC 342. We find that a large fraction of the H II regions show a decreasing value of this ratio as the galactocentric distance increases with increasing galactocentric distance. For a few regions (<5%), their N/O ratio is significantly smaller than that of regions at a similar galactocentric distance. The best fit of the radial distribution of the O/H ratio confirmed a negative gradient (black line in Figure 8). As for oxygen abundance, in Figure 23 we color-coded the H II regions with the residuals of the N/O ratio with respect to the derived radial gradient. We did not find a specific location where there was a larger deficit or enhancement of this ratio. We also did not find a possible correlation between the deficit and morphological features (e.g., an arm, inter-arm, etc.).

To further understand this ratio in the context of galaxy evolution, in Figure 9 we plot the N/O ratio against the oxygen abundance color-coded by their distance. We find that most of the regions, independent of the distance, are clustered in the well-studied linear relation between N/O and O/H (e.g., Belfiore et al., 2017; Espinosa-Ponce et al., 2022). We note that with respect to large samples of H II regions included in a large number of galaxies (e.g., the CALIFA survey Espinosa-Ponce et al., 2022, , see

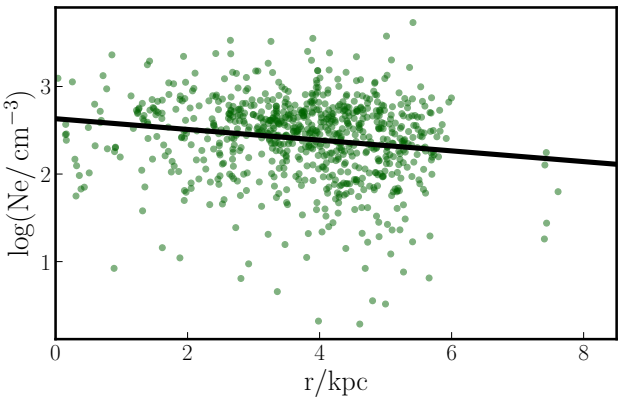

Figure 10. Similar to Figure 8, radial distribution of the electronic density for star-forming regions.

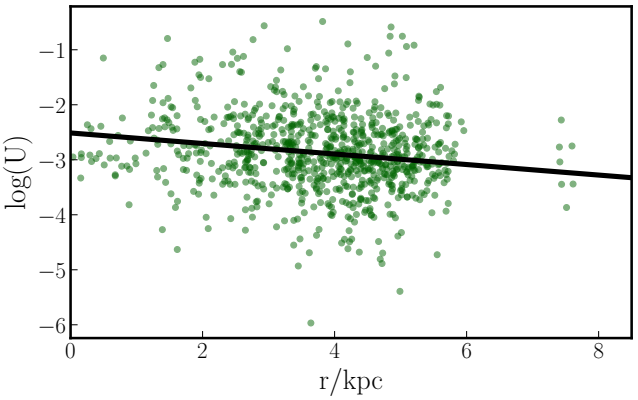

Figure 11. Similar to Figure 8, radial distribution of the ionization parameter for star-forming regions.

cyan-dashed line in Figure 9), those from IC 342 exhibit large metallicities and thus large N/O ratios. In relation to the regions with a large deficit of the N/O ratio, we find that these H II regions cover a wide range of metallicities. In conclusion, the bulk of the H II regions for IC 342 exhibit a similar trend in the N/O-O/H plane as the H II regions in other extragalactic sources. Furthermore, some H II regions in this galaxy show larger values of the oxygen abundance and N/O ratio than the others. These regions appear to follow the linear trend described by large samples of H II surveys. Finally, the underlying reason for the significant deficit of the N/O ratio in H II regions remains unclear.

4.4. Electronic density and Ionization parameter

In Figure 10 we show the radial distribution of the electron density, n_e, for the sample of H II regions where we can measure this physical property. Despite the large scatter, we find that regions at larger galactocentric distances tend to have lower densities than those at closer distances. This is expected, as regions in the center (where the stellar and gas densities are larger) are prone to be under larger pressure than regions at the outskirts (e.g., Barrera-Ballesteros et al., 2021; Barnes et al., 2021). This trend is further quantified by the best radial gradient, which has a negative slope. As for the other properties, we also explored how the residuals of n_e with respect to this gradient were spatially distributed (see Figure 23). We did not find any significant patterns in the spatial distribution of these residuals.

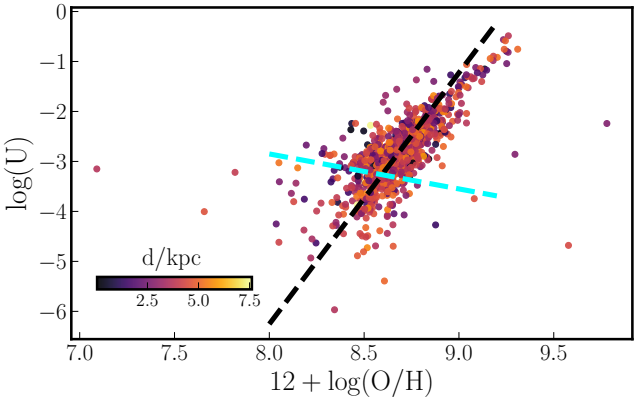

Figure 12. Comparison between the ionization parameter and the oxygen abundance for our sample of star-forming regions. Data points are color-coded with respect to the galactocentric distance. The black dashed line represent the best linear fit to the data, while the cyan dashed line represents the best fit presented in (Espinosa-Ponce et al., 2022).

In Figure 11, we plot the radial distribution of the ionization parameter for our sample of H II regions. Similar to other properties of the H II regions, we find that this parameter decreases as the galactocentric distance of the regions increases. This was confirmed by the negative slope obtained from the best-fit gradient. Similar radial trends have been observed in other nearby galaxies (e.g., Kreckel et al., 2019; Grasha et al., 2022). A significant relationship has been suggested between the oxygen abundance (and N/O ratio) and the ionization parameter for star-forming regions. Initial studies of the properties of H II regions suggested that these two parameters exhibit an anti-correlation, that is, log(U) decreases as the oxygen abundance increases (e.g., Dopita & Evans, 1986). A similar trend has been found using empirical calibrators of log(U) as those used in this study, for a large sample of star-forming regions included in galaxies observed in CALIFA (see, for example, Figure 3 in Sánchez et al., 2015b). The negative radial gradients from these two parameters derived for our sample of H II regions indicate otherwise. To explore the correlation between these two parameters, we plotted the data shown in Figure 12 where these two parameters are color-coded by the galactocentric distance of the regions. As expected, we found a clear positive trend between these two parameters: metal-rich regions have a large ionization parameter. This is further quantified by the slope of the best linear fit between the two properties (black dashed line). This result contrasts with recent characterizations of large samples of H II regions in

the nearby universe. Using the same calibrators for both properties, Espinosa-Ponce et al. (2022) found a negative correlation between these two parameters (see cyan dashed line). However, they noted that for their sample of regions with low abundances ($12+\log(O/H) \lesssim 8.4$), there is indeed a negative trend of $\log(U)$ with $12 + \log(O/H)$ whereas for regions with high abundances, the trend changes to a positive one. They also mentioned that this relationship, contrary to others, is highly dependent on the calibrator of the ionization parameter. As described above, the average oxygen abundance of the regions from IC 342 is larger than that of regions in a larger sample of galaxies, such as that presented by Espinosa-Ponce et al. (2022). Thus, our results are in agreement with those presented in these studies, that is, $\log(U)$ increases with the oxygen abundance for regions with high metallicity. Although there are different possible explanations for the relationship between these two parameters (see a detailed discussion in Ji & Yan, 2022), it is important to keep in mind that we are using empirical calibrators as tracers of these two parameters. In particular, for $\log(U)$ we consider that these empirical calibrators trace the hardness of the ionizing source. However, as discussed by Espinosa-Ponce et al. (2022), these calibrators gauge the excitation level of the ionized gas, which depends on both the hardness and shape of the ionizing source. Finally, we note that similar positive trends have been observed in the 20 nearby galaxies included in the PHANGS-MUSE survey (Groves et al., 2023), suggesting that the differences in the correlations could be caused by resolution effects.

4.5. Kinematic Properties

In Figure 13 we plot the radial distribution of the kinematic properties of the H II regions detected in IC 342. For the systemic velocity (top panel), we used the value reported by (Tully, 1988, that is, 32 km s^{-1}). Regarding the line-of-sight velocity of the H II regions, we find that the north-west regions present a receding velocity, whereas the south-east regions present an approaching velocity. Our results are in agreement with those derived previously for this galaxy using Fabry-Perot observations (Hernandez et al., 2005). Although it is beyond the scope of this study, it is also necessary to explore how the variations in the line-of-sight velocity with respect to the expected circular velocity for a given radius correlate with other physical properties of the galaxy. This would be significantly useful to understand the impact of, for instance, shocks or other non-circular motions in the physical properties of the ISM. Given that a dynamical model is necessary to obtain the curve that best describes the radial distribution of the velocity of the H II regions, we do not attempt to derive a fit. As mentioned above, this is beyond the scope of this study.

The bottom panel of Figure 13 we show the radial distribution of the velocity dispersion for our sample of H II regions. As expected for a disk galaxy, the dispersion is small ($\sigma_{H\alpha} \sim 30$ km s^{-1}). Furthermore, there is no evident significant variation in the Hα velocity dispersion with

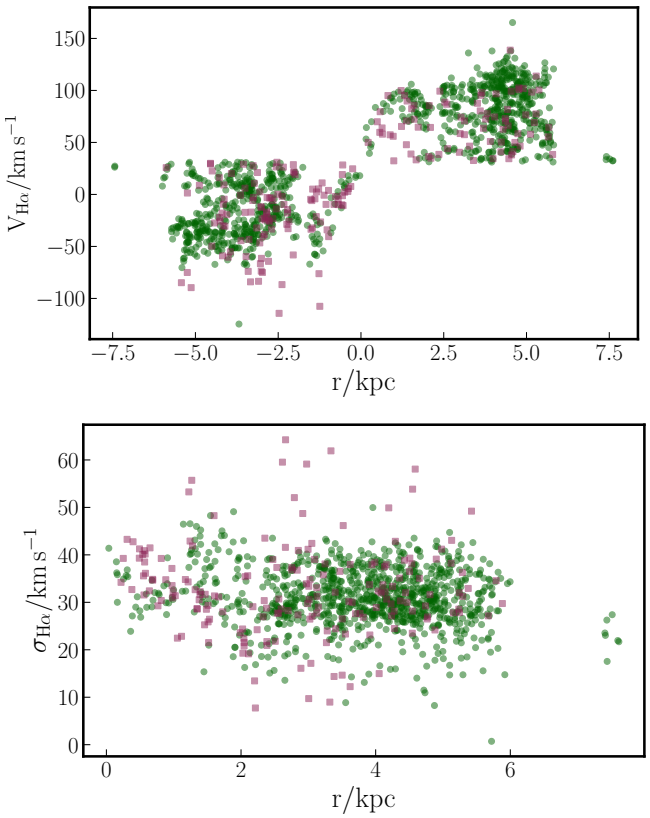

Figure 13. Radial distribution of the systemic velocity and the velocity dispersion of the H II regions (top, and bottom panels, respectively). Similar to previous plots, we segregate the regions between star and non-star forming (green circles and pink squares, respectively) .

respect to the galactocentric distance. We also note that for the outer parts of the galaxy (i.e., r > 2 kpc), the regions with larger Hα velocity dispersion are those that we consider non-star forming. In § 6 we explore whether the velocity dispersion is related to the radial residuals derived for the other physical parameters derived in this study.

5. Hα Luminosity Function

Since the Hα luminosity in an H II region is considered a tracer of the formation of young massive stars, exploring the Hα luminosity function in these regions (HαLF) will trace the massive end of the mass function in galaxies. Thanks to the spatial resolution of the dataset explored in this study, we were able to derive the HαLF for the H II candidates of IC 342, which is one of the closest galaxies where the HαLF has been explored so far. Because this function is basically a histogram of the Hα luminosity function of H II regions, the estimation of the best slope is heavily dependent on how the binning of that histogram is selected. This slope is derived using the brightest H II regions; thus, it is required to select a minimum luminosity (L_{min}), which could vary depending on the adopted binning scheme (e.g., same number of regions per bin or fixed luminosity per bin). Instead of

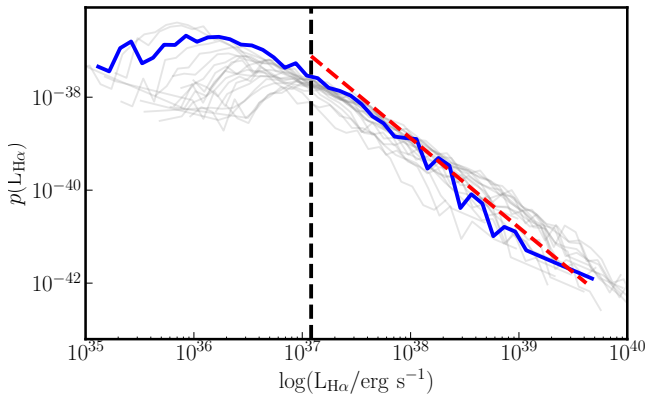

Figure 14. Probability distribution function of the Hα luminosity for the H II regions detected in IC 342 (blue solid line). This distribution function was compared with those derived for galaxies included in the PHANGS-MUSE survey (Santoro et al., 2022, gray solid lines). The red dashed line represents the best fit of the power-law to the dataset. The vertical dashed line represents the minimum luminosity used to derived the fit.

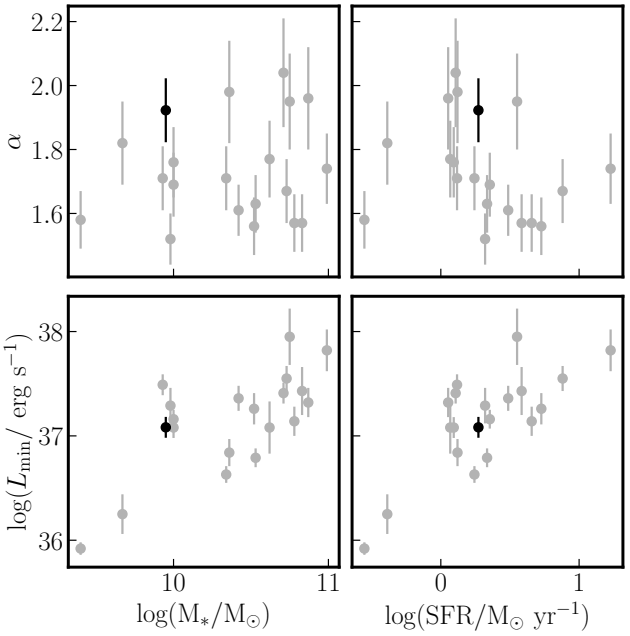

Figure 15. Comparison between the best fit parameters derived for IC 342 (α, and L_{min}; black circles) and those derived for the PHANGS-MUSE galaxies (gray circles). Right panels show these two parameters against the total stellar mass of galaxies while left panels show these parameters against the integrated SFR.

using a histogram, we followed a procedure similar to that presented by Santoro et al. (2022) to derive the HαLF for a sample of 19 galaxies included in the PHANGS-MUSE survey. Following a similar methodology also allows us to provide a direct comparison between nearby galaxies observed with IFS. In a few words, the method does not depend on any binning scheme, as it models the probability distribution function (PDF), $p(L)$, using a power-law of the form:

$$p(L) = (\alpha - 1)\, L_{min}^{\alpha-1}\, L^{-\alpha} \ \text{ with } \ L \geq L_{min}. \qquad (1)$$

The best fit of the HαLF was obtained using the Python package POWERLAW (Alstott et al., 2014). This algorithm uses a maximum likelihood estimation method in combination with Kolmogorov-Smirnov statistics to derive the best values of L_{min} and α, providing a robust statistical way to derive these parameters (Clauset et al., 2009; Santoro et al., 2022). To derive the uncertainties for these parameters, we ran 1000 realizations of the HαLF varying the values of the fluxes of the Hα emission within their uncertainties.

In Figure 14, we plot the PDF of the H II regions detected in IC 342 (blue solid line), the best fit of the HαLF (red dashed line), and the PDFs derived for the PHANGS-MUSE galaxies from (Santoro et al., 2022, gray lines). The PDF of IC 342 covers a similar range of luminosities as those derived for the PHANGS-MUSE sample. Its shape is also similar to that of some galaxies. The find that the best-fit values for IC 342 are $\alpha = 1.9 \pm 0.1$ and $\log(L_{min}/\mathrm{erg\ s^{-1}}) = 37.1 \pm 0.1$. We also compared these parameters with those derived for the PHANGS-MUSE galaxies. In Figure 15 we plot α and L_{min} against the integrated stellar mass and SFR (left and right panels, respectively) for the PDFs presented by (Santoro et al., 2022, grey circles) and those derived in this study for IC 342. In general, we observe that the slope of the HαLF for IC 342 and the value of L_{min} are within the dynamical range of those derived for nearby galaxies. However, we note that IC 342 exhibits one of the steepest slopes compared to those derived for the PHANGS-MUSE galaxies. This is evident for galaxies with similar stellar masses (i.e., $\log(M_*/M_\odot) \sim 10$) and SFR. In contrast, L_{min} is in the average of the values of other galaxies and follows a similar trend as the luminosities derived from the PHANGS-MUSE galaxies, as they increase with both the stellar mass and the SFR.

6. Correlation with residuals from radial trends

In § 4 we describe the radial trend of the derived properties of the H II regions in IC 342. As mentioned in that section, it is important to explore whether the correlations between the parameters still exist after removing the radial trend of these parameters. In Figure 16, we plot the correlation matrix for the radial residuals of the parameters described in § 4. This plot provides a deeper exploration of the possible relationships that these residuals could have.

From left to right, in the first column of Figure 16 we plot the radial residuals of the explored properties against the Hα luminosity residual, $\Delta L_{H\alpha}$. For $\Delta L_{H\alpha}$, we found that it strongly correlated with the residuals of EW(Hα), $\Delta EW(H\alpha)$. This is expected because the flux

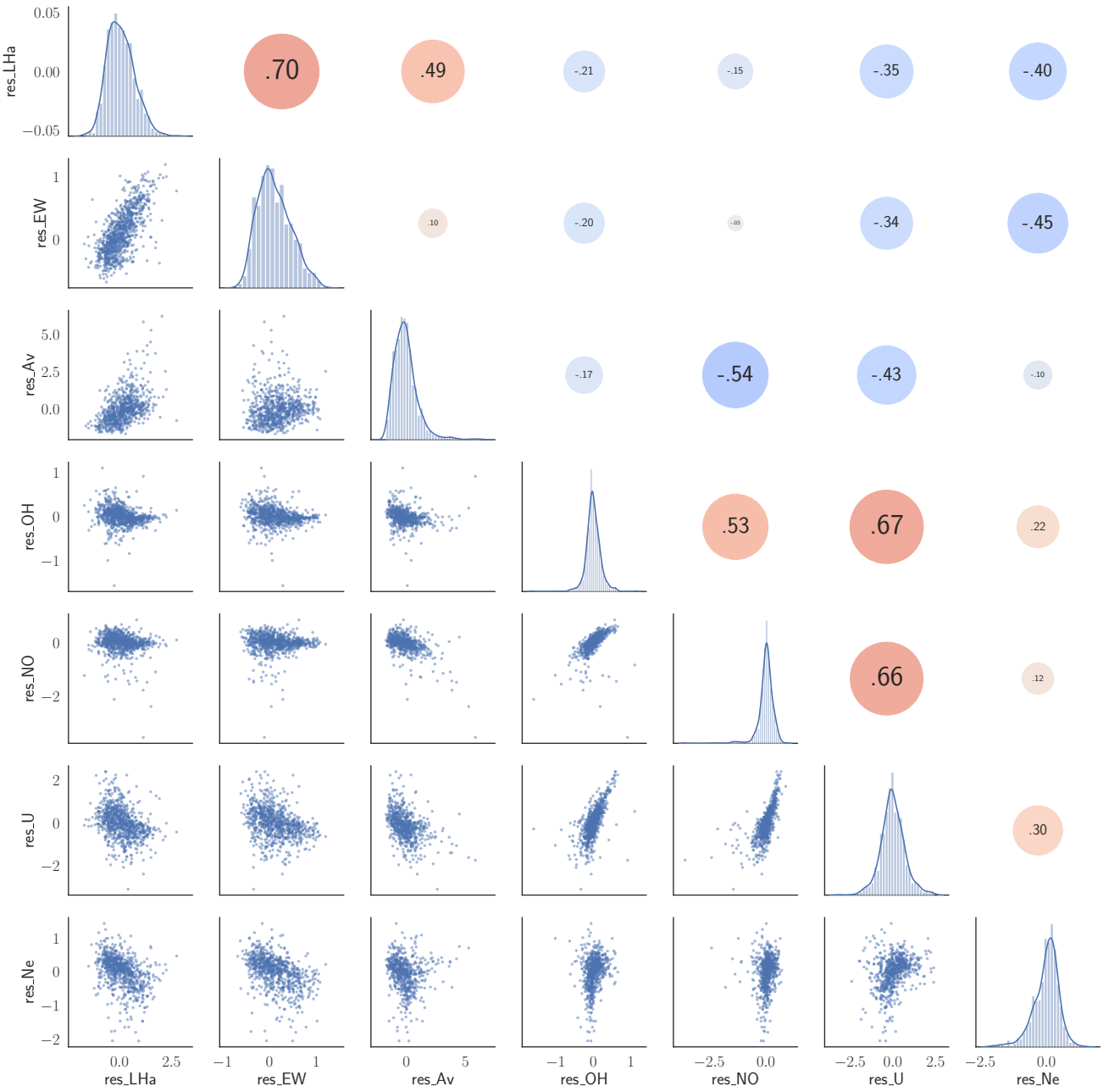

Figure 16. Correlation matrix comparing the radial residuals of the different physical properties of the regions considered as star-forming. The diagonal panels show the histogram of the residuals whereas the lower off-diagonal panels show the distributions and the upper off-diagonal panels show the Pearson's correlation coefficient for parameters corresponding to the transposed panel.

of the Hα emission line is significantly larger than the adjacent continuum for regions with a large Hα luminosity. Furthermore, the fact that we find this strong correlation using the radial residuals suggests that this correlation is independent of the galactocentric distance. In addition, the other positive correlation we find for Δ $L_{H\alpha}$is with the residuals of the optical extinction, $\Delta(A_V)$. As mentioned in Barrera-Ballesteros et al. (2020), the optical extinction in nearby galaxies traces the amount of cold gas at kpc scales. Thus, because these two parameters are usually associated with the current star-formation and the amount of available cold gas to form new stars, we could think that this is a manifestation of the well-known star-formation law (e.g., Kennicutt & Evans, 2012). For the residuals related to the chemical enrichment of the H II regions, we do not find significant correlations (i.e., $\Delta O/H$, and $\Delta N/O$, respectively). This is relevant, as it indicates that the luminosity of a given H II region does not strongly correlate

with the chemical abundance of the ISM, suggesting that the chemical content of star-forming regions is associated with the chemical enrichment from previous generations of stars (for example, Sánchez et al., 2015b). However, previous studies have suggested significant correlations between $L(\mathrm{H}\alpha)$ and the residuals of the oxygen abundance, suggesting the influence of star formation with chemical enrichment within H II regions (e.g., Kreckel et al., 2019). Finally, we found mild negative correlations between $\Delta\,\mathrm{L}_{\mathrm{H}\alpha}$ and the radial residuals of the ionization parameter and electronic density. Although we find that these three parameters present a negative radial gradient, in other words, they follow the same trend with galactocentric distance, once we remove the contribution from the radial gradient, these two properties decrease as $\Delta\,\mathrm{L}_{\mathrm{H}\alpha}$ increases. At first glance, it is not clear why for a given galactocentric distance brighter regions in Hα tend to have lower densities.

Contrary to $\Delta\,\mathrm{L}_{\mathrm{H}\alpha}$, for the residuals of EW(Hα), we do not find significant correlations with other radial residuals, except for the one derived for the electronic density. Our analysis indicates that for a given galactocentric distance, regions with large EW(Hα) tend to have lower electron densities. As for $\Delta\,\mathrm{L}_{\mathrm{H}\alpha}$, it is not clear why regions associated with large star-formation activity are less dense than those where star-formation is reduced.

For the radial residuals of the optical extinction, $\Delta(A_V)$, we found that they mainly anti-correlate with the residuals of the N/O ratio and the ionization parameter (panels in the third column from left to right in Figure 16). If N/O traces the ratio between the yield produced by old over young stars in the ISM, this result suggests that regions with chemical enrichment mostly from young stars have a larger extinction for a given galactocentric radius. This is quantitatively in agreement with the large correlation that we found between $\Delta\,\mathrm{L}_{\mathrm{H}\alpha}$ and $\Delta(A_V)$. Regarding the anti-correlation between $\Delta(A_V)$ and the residual of the ionization parameter, it could be that regions with larger amounts of dust hamper the strength of ionization. As mentioned above, the empirical calibrator that we used traces both the hardness and strength and spectral shape of the ionization source.

For the radial residuals of the oxygen abundance, $\Delta\,\mathrm{O/H}$, we find strong and similar relations to those derived previously between the oxygen abundance, N/O ratio, and ionization parameter (see Figures 9, and 12, respectively). These results suggest that these relations are independent of galactocentric distance. Regarding the residuals of the N/O ratio, as for the case of $\Delta\,\mathrm{O/H}$, we also found a significant correlation between this residual and that derived for the ionization parameter. Finally, we note that the radial residuals of the ionization parameter have a mild but present correlation with the electronic density.

As mentioned in § 4.5, we explore how the residuals of the physical relations correlate with or not with the velocity dispersion derived from Hα emission line width, $\sigma_{\mathrm{H}\alpha}$. In Figure 17, we compared the radial residuals against $\sigma_{\mathrm{H}\alpha}$. We find weak but existing anti-correlations with the other parameters derived from the Hα emission line (i.e., $\Delta\,\mathrm{L}_{\mathrm{H}\alpha}$, and ΔEW(Hα), respectively). This suggests that for a given region located in a given galactocentric distance, the smaller $\sigma_{\mathrm{H}\alpha}$, the brighter the luminosity of that region; similarly for ΔEW(Hα). This suggests that dynamically cold regions are more prone to forming new stars. We also found a mild negative correlation with the radial residual of the extinction, $\Delta\mathrm{A_V}$. This again suggests that regions with a large amount of dust, thus cold gas, are those with the lowest velocity dispersion for a given galactocentric distance. In contrast to these parameters, we found that the parameters related to the chemical abundance and ionization of the ISM mildly correlated with $\sigma_{\mathrm{H}\alpha}$. In particular, we find that $\sigma_{\mathrm{H}\alpha}$ appears to increase with the radial residual of the oxygen abundance, $\Delta\mathrm{O/H}$ suggesting that regions with large velocity dispersion are enriched in comparison to dynamically cold regions.

7. Discussion and conclusions

In this article, we explore the physical properties at sub-kpc scales of H II regions of the nearby galaxy IC 342. This study was made possible by the Integral Field Unit observations provided by the MaNGA survey. These observations, along with the data analysis pipeline devoted to the SDSS-V Local Volume Mapper (LVM), allowed us to measure the properties of the ionized gas in H II-region candidates. In comparison to other regions from large IFS surveys (such as AMUSING++), these candidates are similar in a BPT diagram, as well as in the radial distribution of their properties (see Figure 2). Depending on the explored property, IC 342 exhibits positive, flat, or negative gradients (e.g., the EW(Hα), Hα luminosity, or N/O ratio, respectively). Using a large heterogeneous set of oxygen abundance calibrators, we find that, despite the large scatter, on average, the radial gradient of the oxygen abundance for the star-forming regions in IC 342 is close to zero (see Figures 6 and 7). Other properties, such as the electron density and ionization parameter, exhibit trends similar to those derived for large samples of H II regions. Regarding the kinematic properties of these H II regions, we find that the velocity dispersion for each H II region is relatively flat across the extension of the galaxy ($\sigma_{H\alpha} \sim 30\,\mathrm{km\,s^{-1}}$). We also find that the probability distribution function of the HαLF of IC 342 is similar to that derived for other nearby galaxies (see Figure 14). Finally, in § 6 we study the possible relationships among the residuals from the radial distribution of the physical properties. Our analysis shows that, in general, the relations among different physical parameters are independent of the radial distribution of the H II regions.

Currently, there are IFU observations of thousands of galaxies, thanks to the MaNGA survey (Bundy et al., 2015). Thus, it is worth asking how the radial properties we derive for IC 342 compare to those derived for this sample of galaxies. In particular, one can ask how the oxygen

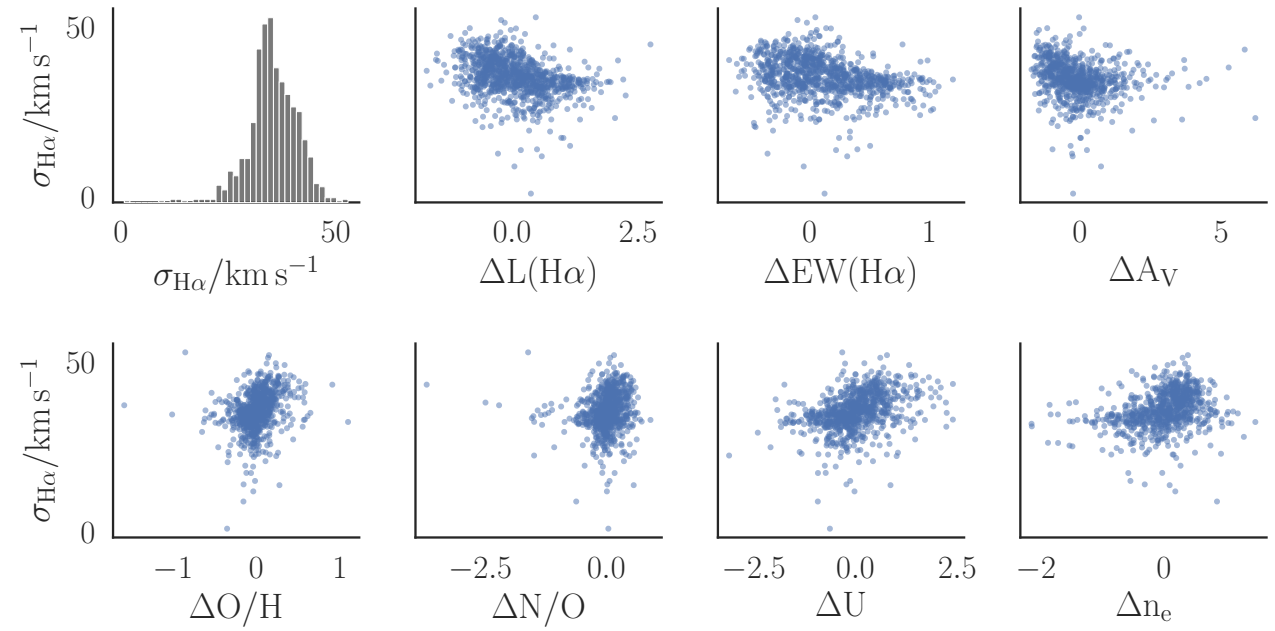

Figure 17. Comparison of the Hα velocity dispersion of the H II regions with the residuals from the different physical properties derived from the ionized gas presented in this study.

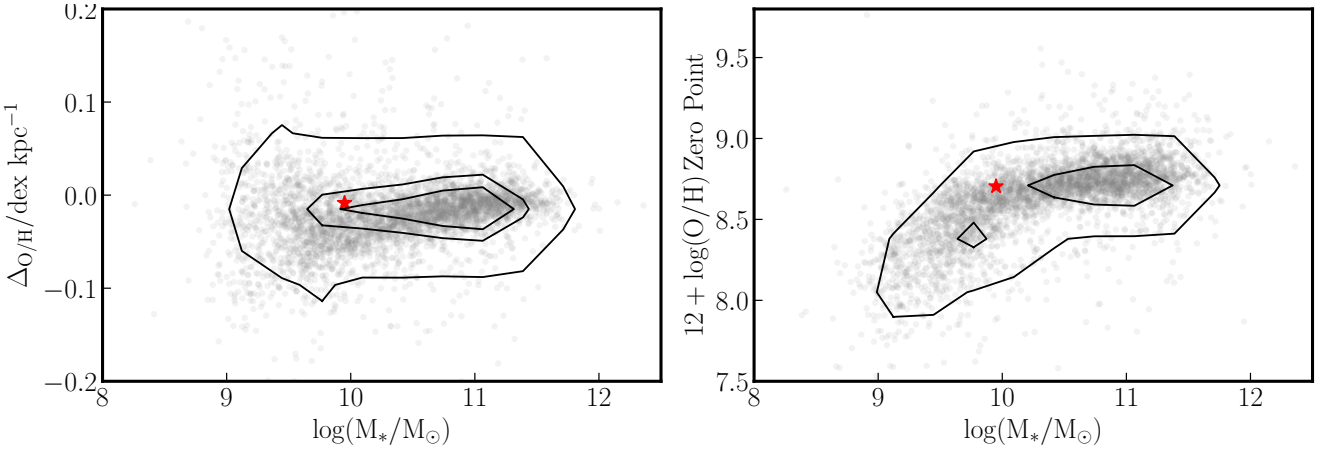

Figure 18. Comparison of the gradient (left-panel) and zero-point (right-panel) of the best of the radial distribution of the oxygen abundance derived in § 4.2 (red star) with those derived for 7533 galaxies included in the MaNGA survey (gray data points).

abundance gradient of the stellar mass of IC 342 compares with those derived from the MaNGA survey, as shown in Figure 18. In the left and right panels of this figure, we compare the slope and zero-point derived for IC 342 in § 4.2 using the Ho calibrator (red star) with those derived for 7533 galaxies drawn from the MaNGA survey (Barrera-Ballesteros et al., 2023)[2], respectively. We find that for the stellar mass of IC 342 the slope and zero-point of the oxygen abundance gradient are similar to those of galaxies with similar stellar masses in the MaNGA survey. In other words, IC 342 shares similar radial properties, at least in its oxygen abundance distribution, with galaxies of similar mass in the nearby universe. This evidence, along with the results from § 5 indicates that IC 342 has similar properties to those reported for other nearby galaxies. Thus, this encourages studies in other galaxies, particularly in the local universe (with higher spatial resolution), to quantify the role of angular resolution in setting the spatially resolved properties of galaxies.

[2]We note that for the comparison between IC 342 and the MaNGA survey, we derived a single gradient for the oxygen abundance. Furthermore, we quantified this gradient in units of dex/kpc. This is slightly different from our previous study, where we used a piece-wise analysis and the slope was measured in units of dex/R_{eff}.

Acknowledgments

J.B-B acknowledges funding from grant IA-101522 (DGAPA-PAPIIT, UNAM) and support from the DGAPA-PASPA 2025 fellowship (UNAM). L.C. thanks the support from the grant IN103820 (DGAPA-PAPIIT, UNAM). J.B-B thanks Laurent Drissen and Carmelle Robert for their useful comments that helped improve the quality of this article. KK gratefully acknowledges funding from the Deutsche Forschungsgemeinschaft (DFG, German Research Foundation) in the form of an Emmy Noether Research Group (grant number KR4598/2-1, PI Kreckel) and the European Research Council's starting grant ERC StG-101077573 ("ISM-METALS"). This research made use of Astropy,[3] a community-developed core Python package for Astronomy (Astropy Collaboration et al., 2013, 2018).

Funding for the Sloan Digital Sky Survey IV has been provided by the Alfred P. Sloan Foundation, U.S. Department of Energy Office of Science and the Participating Institutions.

SDSS-IV acknowledges the support and resources from the Center for High Performance Computing at the University of Utah. The SDSS website is www.sdss.org.

SDSS-IV is managed by the Astrophysical Research Consortium for the Participating Institutions of the SDSS Collaboration including the Brazilian Participation Group, the Carnegie Institution for Science, Carnegie Mellon University, Center for Astrophysics | Harvard & Smithsonian, the Chilean Participation Group, the French Participation Group, Instituto de Astrofísica de Canarias, The Johns Hopkins University, Kavli Institute for the Physics and Mathematics of the Universe (IPMU) / University of Tokyo, the Korean Participation Group, Lawrence Berkeley National Laboratory, Leibniz Institut für Astrophysik Potsdam (AIP), Max-Planck-Institut für Astronomie (MPIA Heidelberg), Max-Planck-Institut für Astrophysik (MPA Garching), Max-Planck-Institut für Extraterrestrische Physik (MPE), National Astronomical Observatories of China, New Mexico State University, New York University, University of Notre Dame, Observatário Nacional / MCTI, The Ohio State University, Pennsylvania State University, Shanghai Astronomical Observatory, United Kingdom Participation Group, Universidad Nacional Autónoma de México, University of Arizona, University of Colorado Boulder, University of Oxford, University of Portsmouth, University of Utah, University of Virginia, University of Washington, University of Wisconsin, Vanderbilt University, and Yale University.

APPENDICES

A. Spatial distribution of brightest emission lines

In § 2 we describe how the LVM-DAP can extract maps of the physical properties of the ionized gas emission. In Figure 19 we present the maps of the brightest four emission lines in the optical: Hα, Hβ, [N II], [O III] (from left to right, top to bottom). These maps are color-coded to the same scale, so it is easy to see that the two brightest lines are Hα, and [N II]. The weakest emission among them is [O III]; however, it is evident that the nuclear emission is brighter than the rest of the galaxy. Despite the difference in brightness, these emission lines followed a spatial distribution similar to that of the Hα emission. We used the information from these emission lines to derive the physical properties of the H II regions.

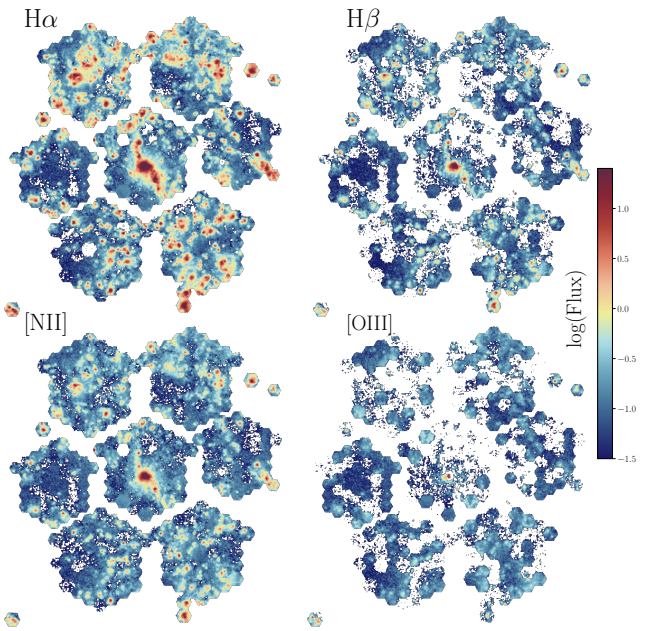

Figure 19. Maps of the flux from the four brightest emission lines in the optical measured from the MaNGA observations. From top to bottom, left to right, the Hα, Hβ, H II, and [O III] emission lines are shown. The flux units are the same for all the lines: 10^{-17}erg cm^{-2} s^{-1}.

[3] http://www.astropy.org

B. Spatial distribution of physical properties from candidates

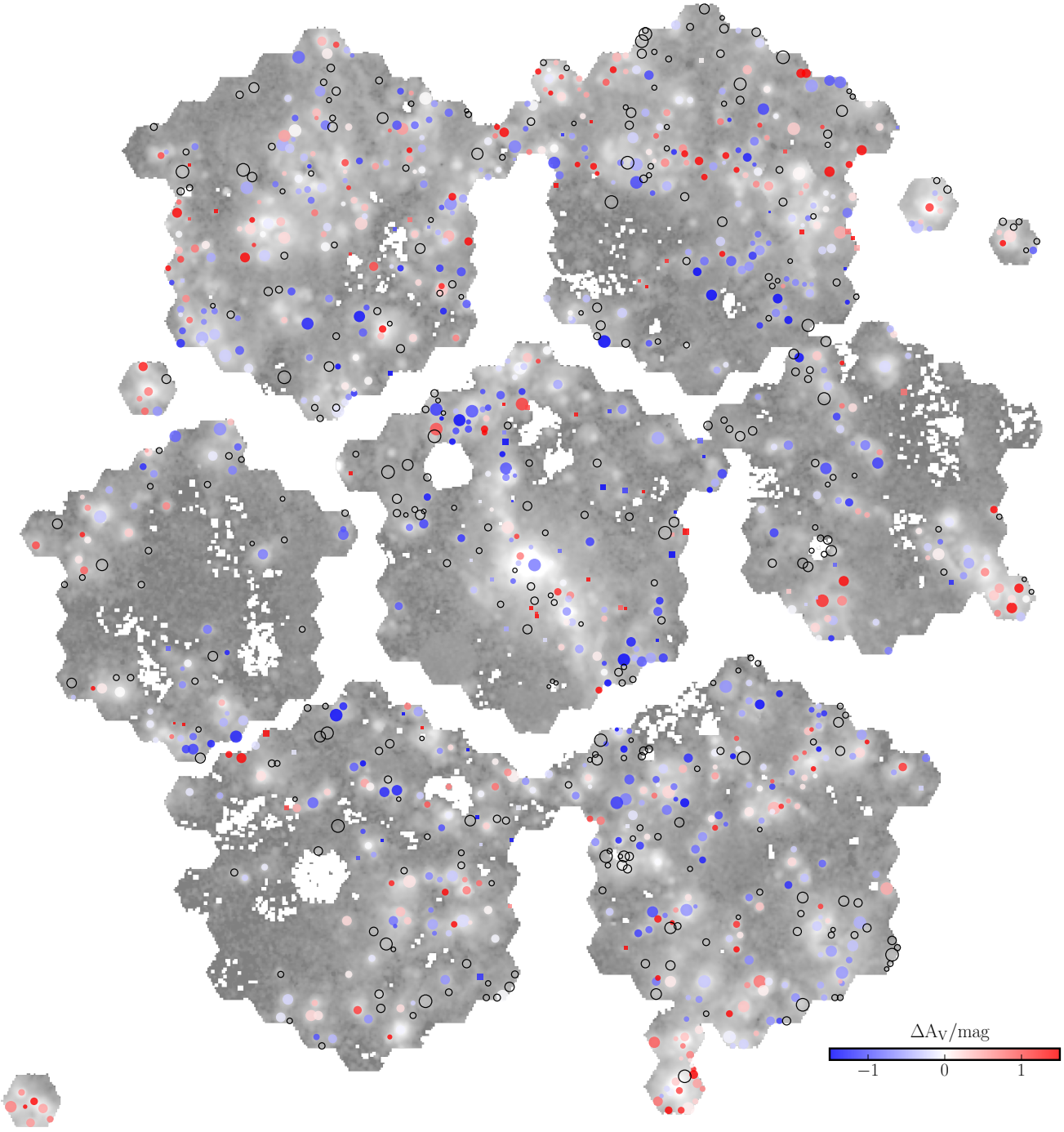

Figure 20. Similar to Figure 1, with the H II candidates color-coded by the residual with respect to the gradient of A_V derived in § 4.1. The empty regions represent those where $H\alpha/H\beta < 2.86$. Circles and squares represent star- and non-star-forming regions, respectively, according to the selection criteria described in § 3.3.

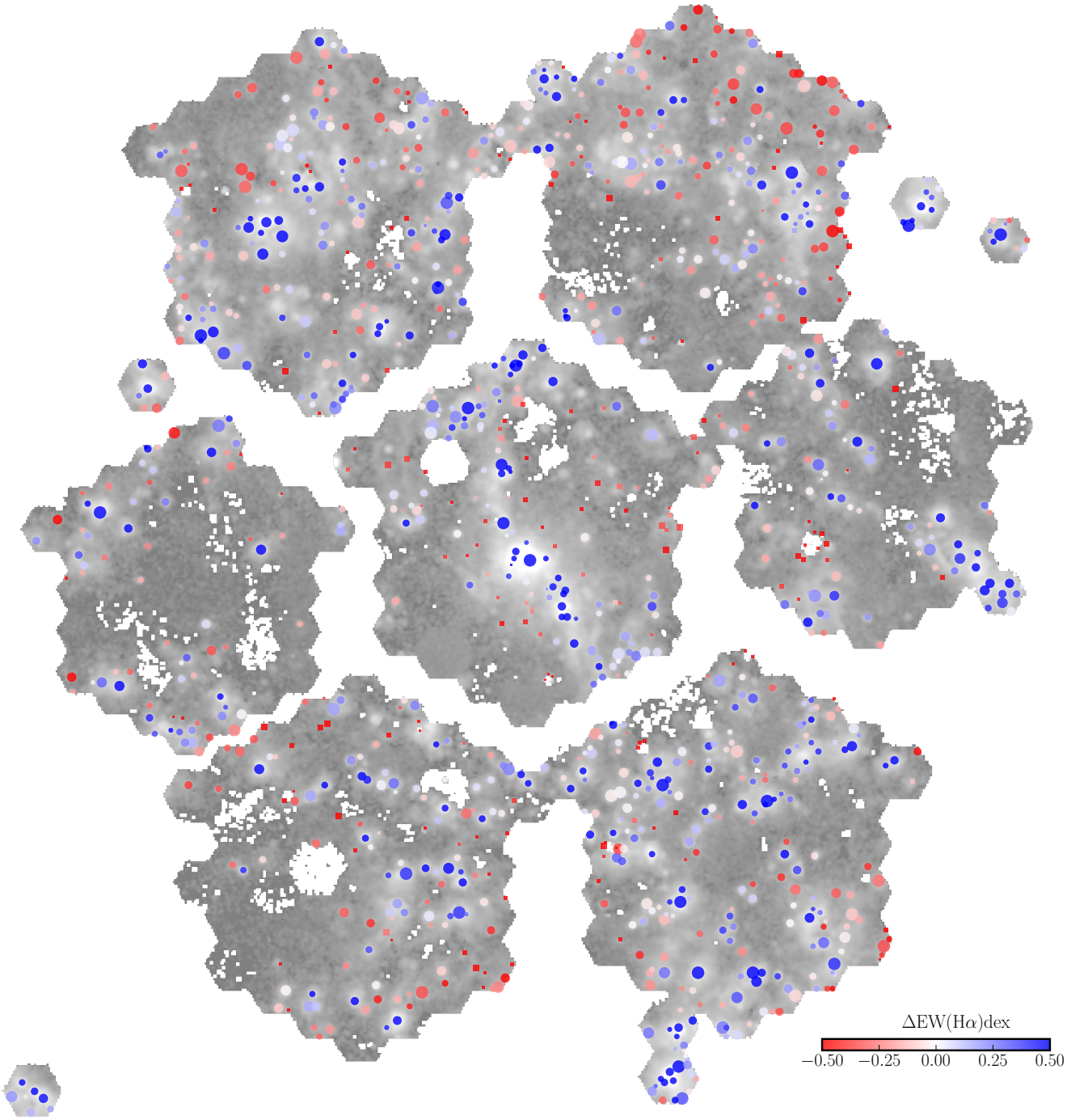

Figure 21. Similar to Figure 1, with the H II candidates color-coded by the residual with respect to the radial gradient of EW(Hα) derived in § 4.1. Circles and squares represent the star and non-star forming regions, respectively, according to the selection criteria described in § 3.3.

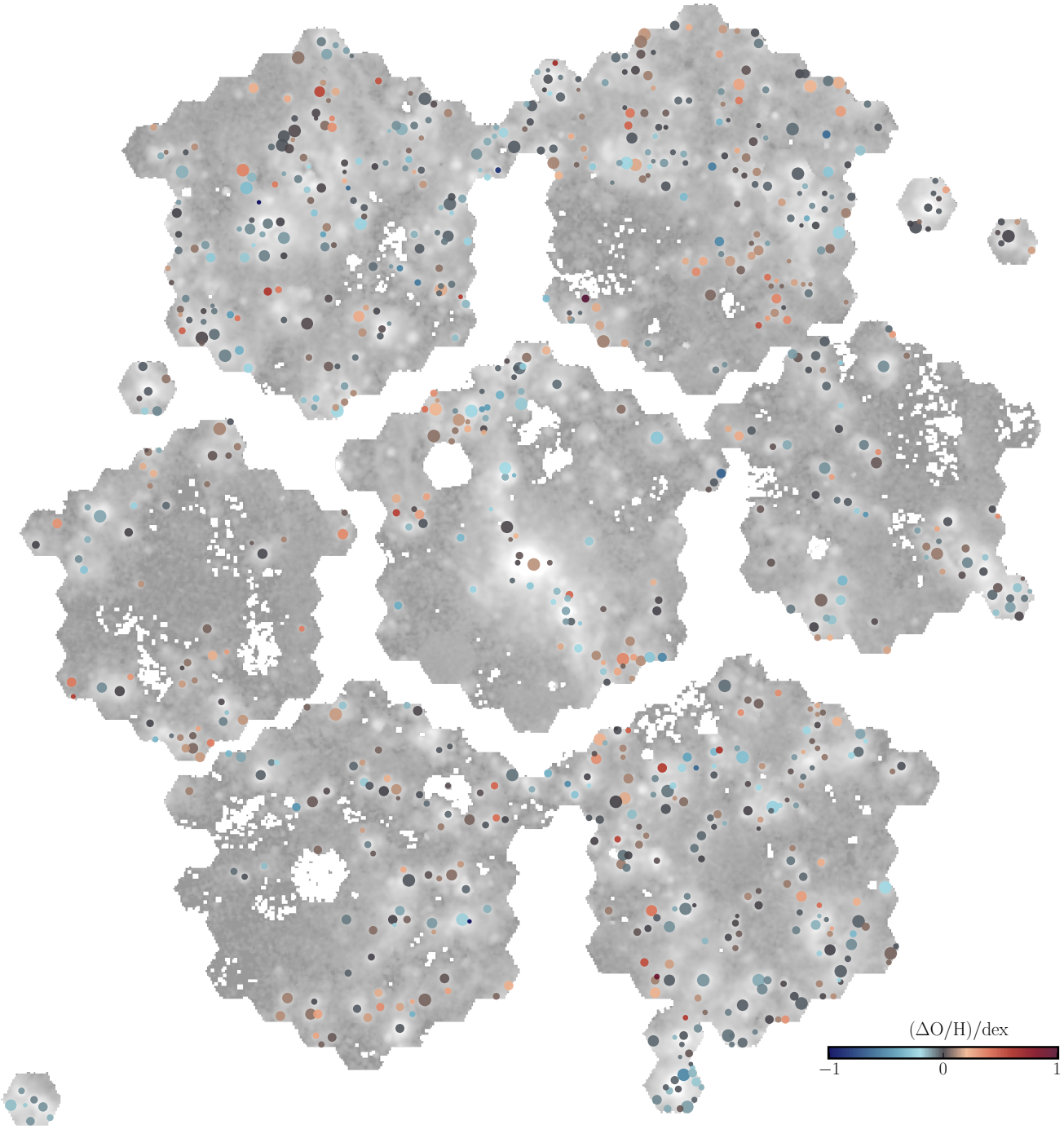

Figure 22. Similar to Figure 1, with the H II candidates color-coded by the residual with respect to the radial gradient of the oxygen abundance derived in § 4.2.

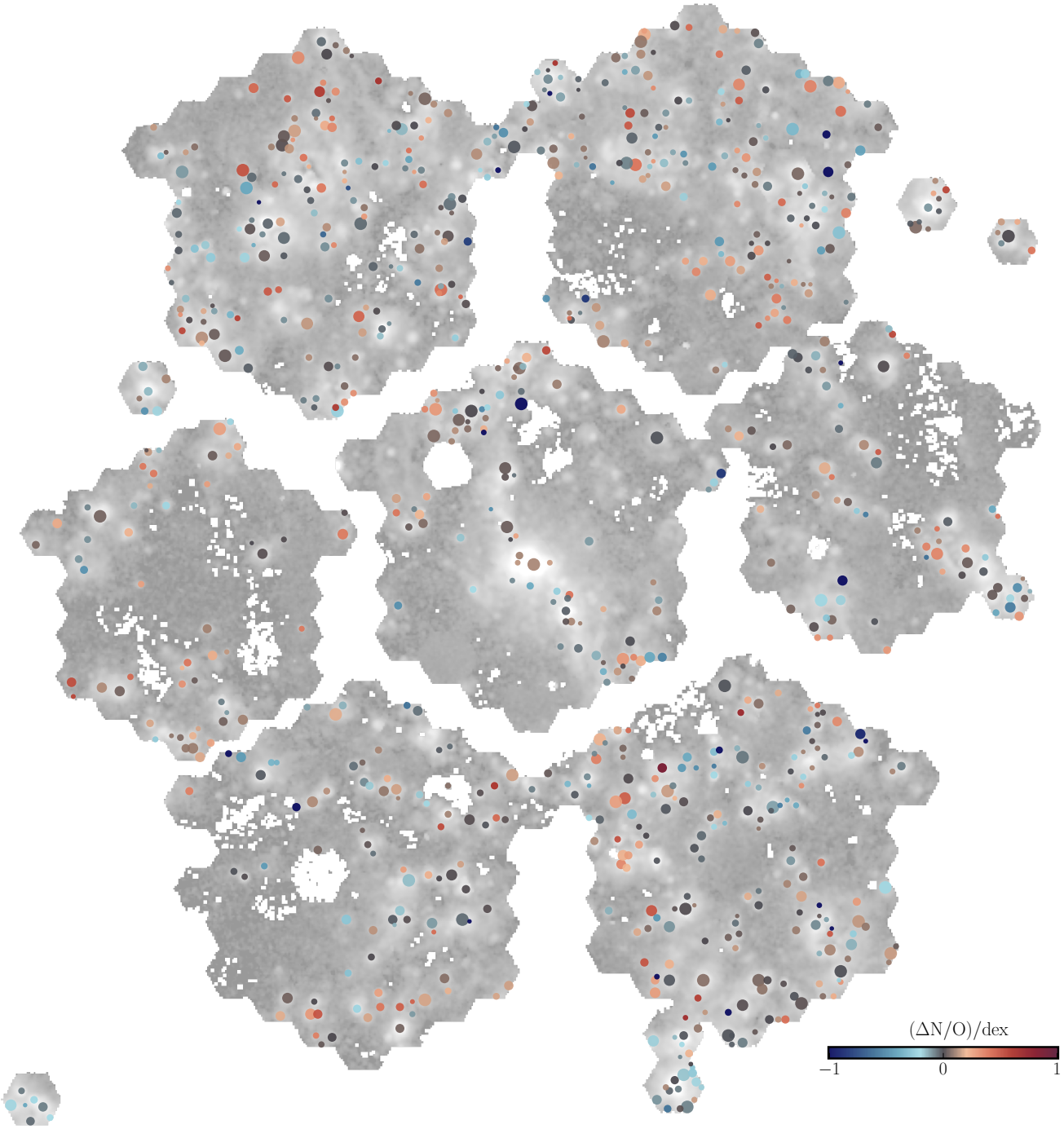

Figure 23. Similar to Figure 1, with the H II candidates color-coded by the residual with respect to the radial gradient of the N/O ratio derived in § 4.3.

References

Alstott, J., Bullmore, E., & Plenz, D. 2014, PLoS ONE, 9, e85777, doi: 10.1371/journal.pone.0085777

Anderson, L. D. 2014, in AAS, Vol. 223, American Astronomical Society Meeting Abstracts #223, 312.01

Astropy Collaboration, Robitaille, T. P., Tollerud, E. J., et al. 2013, A&A, 558, A33, doi: 10.1051/0004-6361/201322068

Astropy Collaboration, Price-Whelan, A. M., SipHocz, B. M., et al. 2018, AJ, 156, 123, doi: 10.3847/1538-3881/aabc4f

Baldwin, J. A., Phillips, M. M., & Terlevich, R. 1981, PASP, 93, 5, doi: 10.1086/130766

Barnes, A. T., Glover, S. C. O., Kreckel, K., et al. 2021, MNRAS, 508, 5362, doi: 10.1093/mnras/stab2958

Barrera-Ballesteros, J. K., Utomo, D., Bolatto, A. D., et al. 2020, MNRAS, 492, 2651, doi: 10.1093/mnras/stz3553

Barrera-Ballesteros, J. K., Sánchez, S. F., Heckman, T., et al. 2021, MNRAS, 503, 3643, doi: 10.1093/mnras/stab755

Barrera-Ballesteros, J. K., Sánchez, S. F., Espinosa-Ponce, C., et al. 2023, RMxAA, 59, 213, doi: 10.22201/ia.01851101p.2023.59.02.06

Belfiore, F., Maiolino, R., Tremonti, C., et al. 2017, MNRAS, 469, 151, doi: 10.1093/mnras/stx789

Bigiel, F., Leroy, A., Walter, F., et al. 2008, AJ, 136, 2846, doi: 10.1088/0004-6256/136/6/2846

Blanton, M. R., Bershady, M. A., Abolfathi, B., et al. 2017, AJ, 154, 28, doi: 10.3847/1538-3881/aa7567

Bradley, T. R., Knapen, J. H., Beckman, J. E., & Folkes, S. L. 2006, A&A, 459, L13, doi: 10.1051/0004-6361:20066151

Bundy, K., Bershady, M. A., Law, D. R., et al. 2015, ApJ, 798, 7, doi: 10.1088/0004-637X/798/1/7

Catalán-Torrecilla, C., Gil de Paz, A., Castillo-Morales, A., et al. 2015, A&A, 584, A87, doi: 10.1051/0004-6361/201526023

Cid Fernandes, R., Stasińska, G., Mateus, A., & Vale Asari, N. 2011, MNRAS, 413, 1687, doi: 10.1111/j.1365-2966.2011.18244.x

Cid Fernandes, R., Stasińska, G., Schlickmann, M. S., et al. 2010, MNRAS, 403, 1036, doi: 10.1111/j.1365-2966.2009.16185.x

Clauset, A., Shalizi, C. R., & Newman, M. E. J. 2009, SIAMR, 51, 661, doi: 10.1137/070710111

Croom, S. M., Lawrence, J. S., Bland-Hawthorn, J., et al. 2012, MNRAS, 421, 872, doi: 10.1111/j.1365-2966.2011.20365.x

Crosthwaite, L. P., Turner, J. L., & Ho, P. T. P. 2000, AJ, 119, 1720, doi: 10.1086/301302

D'Agostino, J. J., Poetrodjojo, H., Ho, I. T., et al. 2018, MNRAS, 479, 4907, doi: 10.1093/mnras/sty1676

Della Bruna, L., Adamo, A., Bik, A., et al. 2020, A&A, 635, A134, doi: 10.1051/0004-6361/201937173

Della Bruna, L., Adamo, A., Lee, J. C., et al. 2021, A&A, 650, A103, doi: 10.1051/0004-6361/202039402

Della Bruna, L., Adamo, A., Amram, P., et al. 2022, A&A, 660, A77, doi: 10.1051/0004-6361/202142315

Dopita, M. A., & Evans, I. N. 1986, ApJ, 307, 431, doi: 10.1086/164432

Dottori, H. A., & Copetti, M. V. F. 1989, RMxAA, 18, 115

Drory, N., MacDonald, N., Bershady, M. A., et al. 2015, AJ, 149, 77, doi: 10.1088/0004-6256/149/2/77

Drory, N., Blanc, G. A., Kreckel, K., et al. 2024, arXiv e-prints, arXiv:2405.01637, doi: 10.48550/arXiv.2405.01637

Emsellem, E., Schinnerer, E., Santoro, F., et al. 2022, A&A, 659, A191, doi: 10.1051/0004-6361/202141727

Espinosa-Ponce, C., Sánchez, S. F., Morisset, C., et al. 2022, MNRAS, doi: 10.1093/mnras/stac456

Galbany, L., Anderson, J. P., Rosales-Ortega, F. F., et al. 2016, MNRAS, 455, 4087, doi: 10.1093/mnras/stv2620

Galbany, L., Anderson, J. P., Sánchez, S. F., et al. 2020, in XIV.0 Scientific Meeting (virtual) of the Spanish Astronomical Society, 38

García-Benito, R., Pérez, E., Díaz, Á. I., Maíz Apellániz, J., & Cerviño, M. 2011, AJ, 141, 126, doi: 10.1088/0004-6256/141/4/126

González Delgado, R. M., & Pérez, E. 1997, ApJS, 108, 199, doi: 10.1086/312950

Grasha, K., Chen, Q. H., Battisti, A. J., et al. 2022, ApJ, 929, 118, doi: 10.3847/1538-4357/ac5ab2

Groves, B., Kreckel, K., Santoro, F., et al. 2023, MNRAS, 520, 4902, doi: 10.1093/mnras/stad114

Gunn, J. E., Siegmund, W. A., Mannery, E. J., et al. 2006, AJ, 131, 2332, doi: 10.1086/500975

Hernandez, O., Carignan, C., Amram, P., Chemin, L., & Daigle, O. 2005, MNRAS, 360, 1201, doi: 10.1111/j.1365-2966.2005.09125.x

Ho, I. T. 2019, MNRAS, 485, 3569, doi: 10.1093/mnras/stz649

Hodge, P. W., & Kennicutt, R. C., J. 1983, ApJ, 267, 563, doi: 10.1086/160893

Ishizuki, S., Kawabe, R., Ishiguro, M., Okumura, S. K., & Morita, K.-I. 1990, Natur, 344, 224, doi: 10.1038/344224a0

Jarrett, T. H., Masci, F., Tsai, C. W., et al. 2013, AJ, 145, 6, doi: 10.1088/0004-6256/145/1/6

Ji, X., & Yan, R. 2022, A&A, 659, A112, doi: 10.1051/0004-6361/202142312

Kauffmann, G., Heckman, T. M., White, S. D. M., et al. 2003, MNRAS, 341, 54, doi: 10.1046/j.1365-8711.2003.06292.x

Kennicutt, R. C., & Evans, N. J. 2012, ARA&A, 50, 531, doi: 10.1146/annurev-astro-081811-125610

Kennicutt, R. C., Calzetti, D., Aniano, G., et al. 2011, PASP, 123, 1347, doi: 10.1086/663818

Kewley, L. J., Dopita, M. A., Sutherland, R. S., Heisler, C. A., & Trevena, J. 2001, ApJ, 556, 121, doi: 10.1086/321545

Knapen, J. H. 1998, MNRAS, 297, 255, doi: 10.1046/j.1365-8711.1998.01493.x

Knapen, J. H., Stedman, S., Bramich, D. M., Folkes, S. L., & Bradley, T. R. 2004, A&A, 426, 1135, doi: 10.1051/0004-6361:20041584

Kollmeier, J. A., Zasowski, G., Rix, H.-W., et al. 2017, arXiv e-prints, arXiv:1711.03234, doi: 10.48550/arXiv.1711.03234

Konidaris, N. P., Drory, N., Froning, C. S., et al. 2020, in SPIE, Vol. 11447, Ground-based and Airborne Instrumentation for Astronomy VIII, ed. C. J. Evans, J. J. Bryant, & K. Motohara, 1144718, doi: 10.1117/12.2557565
Kreckel, K., Ho, I. T., Blanc, G. A., et al. 2019, ApJ, 887, 80, doi: 10.3847/1538-4357/ab5115
Kuno, N., Sato, N., Nakanishi, H., et al. 2007, PASJ, 59, 117, doi: 10.1093/pasj/59.1.117
Lacerda, E. A. D., Sánchez, S. F., Cid Fernandes, R., et al. 2020, MNRAS, 492, 3073, doi: 10.1093/mnras/staa008
Lacerda, E. A. D., Sánchez, S. F., Mejía-Narváez, A., et al. 2022, NewA, 97, 101895, doi: 10.1016/j.newast.2022.101895
Lacerda, E. A. D., Cid Fernandes, R., Couto, G. S., et al. 2018, MNRAS, 474, 3727, doi: 10.1093/mnras/stx3022
Law, D. R., Cherinka, B., Yan, R., et al. 2016, AJ, 152, 83, doi: 10.3847/0004-6256/152/4/83
López-Cobá, C., Sánchez, S. F., Moiseev, A. V., et al. 2017, MNRAS, 467, 4951, doi: 10.1093/mnras/stw3355
López-Cobá, C., Sánchez, S. F., Anderson, J. P., et al. 2020, AJ, 159, 167, doi: 10.3847/1538-3881/ab7848
Lugo-Aranda, A. Z., Sánchez, S. F., Barrera-Ballesteros, J. K., et al. 2024, MNRAS, 528, 6099, doi: 10.1093/mnras/stae345
Lugo-Aranda, A. Z., Sánchez, S. F., Espinosa-Ponce, C., et al. 2022, RAS Techniques and Instruments, 1, 3, doi: 10.1093/rasti/rzac001
McCall, M. L., Rybski, P. M., & Shields, G. A. 1985, ApJS, 57, 1, doi: 10.1086/190994
McLeod, A. F., Dale, J. E., Evans, C. J., et al. 2019, MNRAS, 486, 5263, doi: 10.1093/mnras/sty2696
McLeod, A. F., Kruijssen, J. M. D., Weisz, D. R., et al. 2020, ApJ, 891, 25, doi: 10.3847/1538-4357/ab6d63
McLeod, A. F., Ali, A. A., Chevance, M., et al. 2021, MNRAS, 508, 5425, doi: 10.1093/mnras/stab2726
Pilyugin, L. S., & Grebel, E. K. 2016, MNRAS, 457, 3678, doi: 10.1093/mnras/stw238
Pilyugin, L. S., Vílchez, J. M., & Contini, T. 2004, A&A, 425, 849, doi: 10.1051/0004-6361:20034522
Rickard, L. J., & Palmer, P. 1981, A&A, 102, L13
Rousseau-Nepton, L., Martin, R. P., Robert, C., et al. 2019, MNRAS, 489, 5530, doi: 10.1093/mnras/stz2455
Saha, A., Claver, J., & Hoessel, J. G. 2002, AJ, 124, 839, doi: 10.1086/341649
Sanchez, S. in prep, LVM Data Analysis Pipeline
Sánchez, S. F., Kennicutt, R. C., Gil de Paz, A., et al. 2012, A&A, 538, A8, doi: 10.1051/0004-6361/201117353
Sánchez, S. F., Pérez, E., Sánchez-Blázquez, P., et al. 2015a, ArXiv e-prints. https://arxiv.org/abs/1509.08552
Sánchez, S. F., Pérez, E., Rosales-Ortega, F. F., et al. 2015b, A&A, 574, A47, doi: 10.1051/0004-6361/201424873
Sánchez, S. F., Pérez, E., Sánchez-Blázquez, P., et al. 2016, RMxAA, 52, 171. https://arxiv.org/abs/1602.01830
Sánchez, S. F., Mejía-Narváez, A., Egorov, O. V., et al. 2025, AJ, 169, 52, doi: 10.3847/1538-3881/ad93bb
Sánchez-Menguiano, L., Sánchez, S. F., Pérez, I., et al. 2018, A&A, 609, A119, doi: 10.1051/0004-6361/201731486
Santoro, F., Kreckel, K., Belfiore, F., et al. 2022, A&A, 658, A188, doi: 10.1051/0004-6361/202141907
Schlafly, E. F., & Finkbeiner, D. P. 2011, ApJ, 737, 103, doi: 10.1088/0004-637X/737/2/103
Smee, S. A., Gunn, J. E., Uomoto, A., et al. 2013, AJ, 146, 32, doi: 10.1088/0004-6256/146/2/32
Tully, R. B. 1988, JBAA, 98, 316
Vicens-Mouret, S., Drissen, L., Robert, C., et al. 2023, MNRAS, 524, 3623, doi: 10.1093/mnras/stad2154
Yan, R., Tremonti, C., Bershady, M. A., et al. 2016, AJ, 151, 8, doi: 10.3847/0004-6256/151/1/8
Zhu, Y.-N., Wu, H., Li, H.-N., & Cao, C. 2010, RAA, 10, 329, doi: 10.1088/1674-4527/10/4/004
Zibetti, S., Charlot, S., & Rix, H.-W. 2009, MNRAS, 400, 1181, doi: 10.1111/j.1365-2966.2009.15528.x